

# Measurement of the Ratio $G_E^n/G_M^n$ by the Double-polarized ${}^2\text{H}(\vec{e}, e'\vec{n})$ Reaction

May 4, 2012

J.R.M. Annand (spokesperson & contact), D.J. Hamilton, M. Hoek,  
D. Ireland, R. Kaiser, K. Livingston, I.J.D. MacGregor, M. Murray,  
G. Rosner, B. Seitz, J. Sjögren  
*University of Glasgow, Glasgow G12 8QQ, UK.*

B. Wojtsekhowski (spokesperson), K. Allada, A. Camsonne, J.P. Chen,  
P. Degtyarenko, J. Gomez, O. Hansen, D. Higinbotham, C.W. de Jager,  
M. Jones, J. LeRose, R. Michaels, S. Nanda, L. Pentchev, A. Puckett,  
B. Sawatzky  
*Thomas Jefferson National Accelerator Facility, Newport News, VA 23606,  
USA.*

N. Piskunov (spokesperson), S. Basylev, O. Gavrishchuk, D. Kirillov, G.  
Meshcheryakov, J. Mushinsky, A. Nagaytsev, I. Savin, I. Slepnev, V. Slepnev,  
I. Sitnik  
*Joint Institute for Nuclear Research, Dubna, Russian Federation.*

V. Bellini (spokesperson), A. Giusa, F. Mammoliti, F. Noto, G. Russo,  
M.L. Sperduto, C.M. Sutura  
*INFN Catania and University of Catania, Catania, Italy.*

G. De Cataldo, R. de Leo, L. Lagamba, S. Marrone, G. Simonetti, E. Nappi,  
I.J. Vilardi  
*INFN Bari and University of Bari, Bari, Italy.*

D. Nikolenko, I. Rachek, Yu. Shestakov  
*Budker Institute, Novosibirsk, Russian Federation.*

K. Aniol and D.J. Magaziotis  
*California State University, Los Angeles, CA 90032, USA.*

G. B. Franklin, B. Quinn, R. Schumacher  
*Carnegie Mellon University, Pittsburgh, PA 15213, USA.*

W. Boeglin, P. Markowitz, J. Reinhold, M.M. Sargsian  
*Florida International University, Miami, FL 33199, USA*

M. Aghasyan, E. de Sanctis, L. Hasch, L. Lucherini, M. Mirazita, S.A. Pereira,  
P. Rossi  
*INFN, Laboratori Nazionali di Frascati, Frascati, Italy.*

G. Ron  
*Hebrew University of Jerusalem, Jerusalem, Israel*

B. Anderson, A.T. Katramatou, G.G. Petratos  
*Kent State University, Kent, OH 44242, USA.*

A. Glamazdin, R.Pomatsalyuk  
*Kharkov Institute of Physics and Technology, Kharkov 61108, Ukraine.*

R. Perrino  
*INFN Lecce, Lecce, Italy.*

K. Fissum  
*Lund University, Lund, Sweden.*

S. Riordan  
*University of Massachusetts, Amherst MA 01003, USA.*

W. Bertozzi, S. Gilad, A. Kelleher, V. Sulkosky  
*Massachusetts Institute for Technology, Cambridge, MA 02139, USA.*

F. Cusanno  
*Technische Universität München, Garching 85748, Germany.*

J. Calarco, W. Hersman, K. Slifer  
*University of New Hampshire, Durham, NH 03824, USA.*

M. Khandaker, V. Punjabi  
*Norfolk State University, Norfolk, VA 23504, USA.*

B. Vlahovic  
*North Carolina Central University, Durham, NC 03824, USA.*

A. Ahmidouch and S. Danagoulian  
*North Carolina A&T State University, Greensboro, NC 27411, USA.*

E. Cisbani, S. Frullani, F. Garibaldi  
*INFN Rome, gruppo collegato Sanità and Istituto Superiori di Sanità, Rome, Italy.*

F. Meddi and G.M. Urciuoli  
*INFN Rome and University "La Sapienza", Rome Italy.*

M. Capogni  
*INFN Rome, gruppo collegato Sanità and ENEA Casaccia, Rome, Italy.*

A. D'Angelo, C. Schaerf, I. Zonta  
*INFN Sezione Roma Tor Vergata and Università di Roma Tor Vergata, Rome, Italy.*

L. El Fassi, R. Gilman, G. Kumbartzki, R. Ransome, Y. Zhang  
*Rutgers, The State University of New Jersey, Piscataway, NJ 08854, USA.*

F. Sabatie  
*CEA Saclay, Gif-sur-Yvette, France.*

A. Sarty  
*St. Mary's University, Nova Scotia, B3H 3C3, Canada.*

M. Olson  
*St. Norbert College, De Pere, WI 54115, USA.*

O. Chen, N. Bubis, I. Korover, J. Lichtenstadt, E. Piasetzky, I. Pomerantz,  
R. Shneor, I. Yaron  
*Tel Aviv University, Israel.*

G. Cates, D. Day, C. Hanrrety, R. Lindgren, N. Liyanage, V. Nelyubin,  
B. Norum  
*University of Virginia, Charlottesville, VA 22901, USA.*

T. Averett, C. Perdrisat  
*College of William and Mary, Williamsburg, VA 23185, USA.*

S. Abrahamyan, S. Mayilyan, A. Shahinyan, H. Voskanyan  
*Yerevan Physics Institute, Yerevan, Armenia.*

and

**The Hall A Collaboration.**

### Abstract

A double polarized measurement of quasi-elastic electron scattering in the  ${}^2\text{H}(\vec{e}, e'\vec{n})$  reaction is proposed at values of negative four-momentum transfer  $Q^2 = 1.5, 2.0, 2.5, 3.0, 4.0, 6.0$   $(\text{GeV}/c)^2$ . The ratio of electric to magnetic elastic form factors  $G_E^n/G_M^n$  will be extracted from the ratio of transverse and longitudinal components of the spin polarization  $P_x/P_z$ , which is transferred to the recoiling neutron from an incident, longitudinally polarized electron. The experiment will be performed in Hall-A of Jefferson Laboratory, as part of the program to measure the four nucleon Sachs form factors, and will utilize many of the common components of the Super BigBite apparatus. Scattered electrons will be detected in the “BigBite” large acceptance spectrometer and recoiling neutrons in a polarimeter consisting of plastic scintillator analyzers and the “HCAL” hadron calorimeter. The “48D48” dipole will perform neutron spin precession and sweeping of charged background out of the neutron arm acceptance. The array of plastic scintillator bars, in which neutrons will scatter in order to analyze the incident spin orientation, will be a new addition to the Super BigBite apparatus. This experiment will complement experiments E02-013 and E12-09-016, where the struck neutron is polarized in the initial state in a  ${}^3\text{He}$  target. It employs an independent experimental technique to extract a fundamental observable which is highly challenging to measure. In addition the necessary corrections for bound-neutron effects and final state interactions in  ${}^2\text{H}$  and  ${}^3\text{He}$  will be rather different and in principle more straight forward for  $A=2$  system. We estimate, for the employed parametrization of form-factor (BLAST), that the ratio  $G_E^n/G_M^n$  will be measured to a relative (statistical) precision of 2.5 to 5%, up to 4  $(\text{GeV}/c)^2$  and 10% at 6  $(\text{GeV}/c)^2$ . The systematic uncertainty will be  $\sim 3\%$ . A total beam time of 1054 hr to measure the ratio and perform all necessary commissioning and calibration of apparatus is requested.

# Contents

<b>1</b>	<b>Introduction</b>	<b>9</b>
1.1	Physics Motivation . . . . .	10
1.1.1	pQCD Scaling and Scaling Violations . . . . .	11
1.1.2	Dyson-Schwinger Equation Calculations . . . . .	13
1.1.3	Constituent Quark Models . . . . .	13
1.1.4	Lattice QCD . . . . .	15
1.1.5	Generalized Parton Distributions . . . . .	16
1.1.6	Quark Orbital Angular Momentum . . . . .	16
1.1.7	The Form Factors as a Hadronic Model Testing Ground . . . . .	17
<b>2</b>	<b>Observables and Previous Experiments to Access the Form Factors</b>	<b>18</b>
2.1	Rosenbluth Separation . . . . .	19
2.2	Double polarized measurements . . . . .	20
2.2.1	Polarized Beam and Polarized Target . . . . .	20
2.2.2	Polarized Beam and Recoil Polarimetry . . . . .	21
2.3	Nucleon Polarimetry . . . . .	21
2.4	Neutron Analyzing Power at Several GeV/c . . . . .	23
2.4.1	Experimental Data . . . . .	23
2.4.2	The Analyzing Power of Neutron Polarimetry . . . . .	24
2.5	Previous Form Factor Measurements and Proposals . . . . .	26
2.5.1	Unpolarized . . . . .	26
2.5.2	Polarized Target . . . . .	26
2.5.3	Recoil Polarimetry . . . . .	27
2.6	New Elastic Form Factor Measurements at JLab. . . . .	27
2.6.1	Comparison of the Present Proposal to Hall-C Experiment E12-11-009 . . . . .	29
<b>3</b>	<b>Experimental Method</b>	<b>31</b>
3.1	The e' Detector BigBite . . . . .	32
3.2	The Neutron Polarimeter . . . . .	34
3.2.1	The Plastic Scintillator Analyzer Array and Veto Detector . . . . .	35
3.2.2	Forward Detector for Charged-Particle Identification . . . . .	35
3.2.3	The HCAL Hadron Calorimeter . . . . .	35
3.2.4	Rear Detector for Charged-Particle Identification . . . . .	36
3.2.5	The 48D48 Dipole . . . . .	36
3.3	Kinematics . . . . .	38
<b>4</b>	<b>Determination of the Ratio <math>G_E^n/G_M^n</math></b>	<b>39</b>
4.1	Modeling the polarimeter . . . . .	39
4.1.1	The Simulated Response of the Analyzer Block . . . . .	42
4.1.2	The Simulated Response of the Hadron Calorimeter HCAL . . . . .	43
4.1.3	The Simulated Response of the Polarimeter . . . . .	44
4.1.4	Determination of $G_E^n/G_M^n$ from Simulated Azimuthal Asymmetries . . . . .	46
4.2	Background Rates and the Trigger Rate . . . . .	48
4.3	The Quasi-elastic Signal and Background Rejection . . . . .	51
4.4	Systematic Uncertainties . . . . .	53

<b>5</b>	<b>Proposed Measurements</b>	<b>56</b>
5.1	Counting Rate Estimates . . . . .	56
5.2	Beam Time Request . . . . .	57
<b>6</b>	<b>Summary</b>	<b>60</b>

## Foreword: Comments on the Decision of PAC 37

This proposal was submitted originally to PAC 37, where it was deferred. The comments of the PAC are reproduced below, followed by our response.

---

**Comments of PAC 37** *While we applaud the collaboration in proposing this experiment in Hall A using the recoil neutron polarimeter with the combination of BBS and SBS with excellent, proposed precision, the committee is not convinced that this experiment in its proposed four-momentum transfer region, has the high priority to justify approval for the top half of the first 5-year 12-GeV program. This statement is based on the proposed precision and kinematic reach of the already approved Hall A experiment E12-09-016 using a high-luminosity polarized  $^3\text{He}$  target (which also will use the combination of the SBS and BBS), and of the proposed Hall C neutron recoil polarimeter experiment (PR-11-009). However, this proposed experiment may prove to be very valuable and important in the future, should the two aforementioned experiments at higher values of  $Q^2$  discover something unexpected.*

**Measurement and Feasibility:**

- 1) *BigBite spectrometer with gas Cherenkov, trigger scintillators, and preshower-shower counter, trackers. GEM*
- 2) *Super BigBite (SBS) spectrometer (magnet, hadron calorimeter, part of the GEM tracking system).*
- 3) *Neutron polarimeter analyzer (lead shield, veto tiles, the array of plastic scintillator blocks, new components of SBS). The neutron analyzing power  $A_y$  is poorly known at the proposed energies. The collaboration plans to take analyzing power measurement in the near future at Dubna, which is highly recognized and supported by the committee.*
- 4) *Possibly, one additional set of GEM chambers (covering  $40 \times 200 \text{ cm}^2$ ) for BigBite with "fast pixel readout" and FPGA-based trigger processing electronics (to be developed).*

**Issues:**

- 1) *Most components of the SBS arm, such as the neutron polarimeter analyzer and the GEM trackers, as well as some BigBite components, do not exist at this time. Although there does not appear any show stopper for the experiment, this experiment is a new development with a multitude of potential technical and instrumental issues. Detailed technical reviews of the individual subsystems are warranted.*
  - 2) *The spin precession through the SuperBigBite dipole has to be studied in detail to fringe fields, which can directly affect the measured quantity. evaluate the effect of fringe fields, which can directly affect the measured quantity.*
-

**The Response** We are firmly convinced that it is of the utmost importance to measure the ratio  $G_E^n/G_M^n$  with the best possible precision and accuracy. We here propose values of  $Q^2$  starting from  $1.5 \text{ (GeV/c)}^2$  and extending as high as is feasible. This is exactly the kinematic region where di-quark structure would be expected to manifest. A recent flavor separation of neutron and proton factor data [1] shows quite different  $u$  and  $d$ -quark  $Q^2$  dependence, which has been interpreted qualitatively as evidence of a significant di-quark component of the nucleon wave function. The main uncertainties in flavor-separated distributions arise from uncertainties in  $G_E^n$ . This experiment can achieve smaller statistical and systematic uncertainties than any other JLab measurement of  $G_E^n/G_M^n$  at  $Q^2 = 1.5 - 4 \text{ (GeV/c)}^2$  and thus have maximum impact on flavor separation in this crucial kinematic domain.

A broad range of  $Q^2$  will be achieved by Hall-A experiment E12-09-016 using the polarized  $^3\text{He}$  target technique. However, with a  $^3\text{He}$  target it is more difficult to separate the elastic channel from inelastic background, so that inelastic contamination becomes a major source of systematic uncertainty. By contrast, the deuterium target used in this proposal has much cleaner elastic separation, allowing better accuracy to be achieved up to values of  $Q^2 \sim 6 \text{ (GeV/c)}^2$ . This proposal uses the recoil polarimetry technique to measure  $G_E^n/G_M^n$ . Here the major impediment to reaching high values of  $Q^2$  is the falling value of the analyzing power of neutron-proton scattering with increasing incident nucleon momentum. In this respect neutron scattering is considerably less advantageous than proton scattering when one reaches nucleon momenta of several  $\text{GeV/c}$ .

In PR11-001, we proposed to measure up to  $Q^2 = 4 \text{ (GeV/c)}^2$ . In the interim we have refined our analysis of the momentum dependence of the  $n + ^{12}\text{C}$  analyzing power (Sec. 2.4), based on measurements of free  $n - p$  scattering. These results have been used to estimate for this proposal the counting time for kinematic points up to  $Q^2 = 6.0 \text{ (GeV/c)}^2$ . Our plan to measure neutron analyzing power at JINR Dubna has been delayed, since polarized neutron beams are not yet available at the Nuklotron accelerator. However, we believe that our new analysis of the neutron analyzing power is sufficiently accurate to produce reasonable estimates of the obtainable experimental precision. We note that our technique of neutron polarimetry, utilizing a large-acceptance, high-efficiency polarimeter, produces a figure of merit significantly better (Sec. 2.6.1) than the device proposed in experiment E12-09-006.

Regarding instrumentation issues, we note that the most of the apparatus (Sec. 3) is common to other experiments which have been approved and rated. The configuration of BigBite will be very similar to that of  $A_1^n$  (E12-06-122). The neutron polarimeter arm of the present experiment uses the SBS dipole and the HCAL hadron calorimeter, both of which are employed by the measurement of  $G_M^n/G_M^p$  (E12-09-019). The Coordinate Detector, under development for the electron arm of the GEp(5) experiment, will also be suitable as a charged particle identifier before HCAL. The major new piece of apparatus, the highly segmented active analyzer array, is based on well tried plastic scintillator technology and already several major components of this array have been obtained.

The issue of spin precession through the SBS dipole is addressed in Sec. 3.2.5, where we demonstrate that, with good position resolution in the analyzer array, systematic fringe-field effects are well under control.

# 1 Introduction

The understanding of nucleon structure and the nature of quark confinement is one of the central goals facing nuclear physics today. Ninety nine per cent of the nucleon mass, is due to the kinetic and potential energy of the massless gluons and the essentially massless quarks, confined within the nucleon. Thus most of the mass of visible matter is generated dynamically, rather than through the Higgs mechanism. At the  $\sim fm$  scales typical of hadrons, quantum chromodynamics (QCD), the field theory describing the quark-gluon interaction, is too strong to be solved by perturbative methods (pQCD) and the understanding of non-perturbative QCD remains a pivotal area of theoretical physics.

Since the days of Hoffstadter [2], the elastic form factors have provided vital insight into nucleon structure. These are measured in electron scattering and at small values of  $Q^2$  (the negative of the squared, four momentum transfer) the Fourier transforms of the Sachs electric ( $G_E$ ) and magnetic ( $G_M$ ) form factors can be interpreted as the charge and magnetization densities respectively. Form factor measurements provided an early determination of the size of the proton and high precision studies of the proton remain a core activity of hadron physics. Neutron measurements are more difficult and consequently neutron data generally have poorer precision and a limited kinematic reach.

Fig.1 contains a representation of the charge density of the neutron computed from the 2007 world data set on  $G_E^n$ . The central core is positive, while the more diffuse outer region is negative, consistent with a proton-like core surrounded by a negative pion cloud. Several nucleon models incorporate the pion-cloud idea, which necessarily represents a five-quark state, a configuration that is suppressed when  $Q^2 \gg \Lambda_{\text{QCD}}^2$ . As  $Q^2$  increases relativistic effects limit the degree to which form factors may be interpreted as Fourier transforms of densities, but none the less attempts to account for relativity in the laboratory frame have been conducted [3, 4].

Transverse quark charge densities (Fig. 1) have been computed in a light-front reference frame [5] from the Dirac and Pauli form factors, obtained using empirical fits to the Sachs form factors. For a nucleon in a state of definite helicity the transverse density distribution, obtained from the Dirac form factor, is circularly symmetric. The Pauli form factor relates to a nucleon in a transverse spin state, and for polarization along the  $x$ -axis the transverse charge density is clearly displaced in the  $y$  direction.

One of the critical factors driving progress in understanding nucleon structure is the availability of high precision experimental results over a broad range of  $Q^2$ . The higher  $Q^2$  domain is relatively unexplored and thus has immense potential to assess different nucleon structure models. There the short-range behavior of the nucleon can be revealed, and the structure itself becomes simpler and easier to understand. The  $Q^2$  dependence of  $G_E^p/G_M^p$  has generated more theoretical papers than any other result to come out of Jefferson Laboratory (JLab) and there is considerable anticipation regarding new results that push both  $G_E^p/G_M^p$  and  $G_E^n/G_M^n$  to higher values of  $Q^2$ . Measurements of the elastic form factors remain a major source of information about quark distributions at small transverse distance scales. Indeed many theoretical approaches to understanding nucleon structure, including phenomenological models, GPD analyses and lattice QCD calculations, require input and constraint from form-factor measurements.

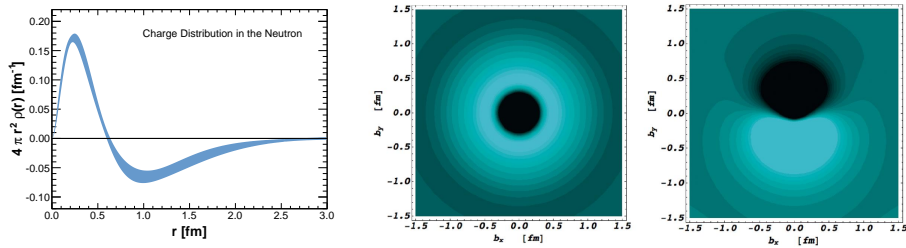


Figure 1: Left: Radial dependence of the neutron charge density computed from the 2007 world data on  $G_E^n$ . Middle: Transverse quark charge density for neutron with definite helicity. Right: Transverse quark charge density for neutron polarized along  $x$ -axis. Transverse distributions from [5]

The Super-Bigbite-Spectrometer (SBS) experimental program already has three approved measurements of nucleon elastic form factors [6, 7, 8], which will use the results of E12-07-108 [9]. The latter will measure  $G_M^p$  up to  $17.5 (\text{GeV}/c)^2$  using the Hall-A HRS spectrometers to achieve a 1-2% measurement of the electron-proton elastic scattering cross section. Thus extraction of absolute values of  $G_M^n$ ,  $G_E^p$  and  $G_E^n$  from ratio measurements will be possible. A major strength of the program in Hall-A is the ability to measure all of the ground-state electromagnetic form factors, with sufficient accuracy and reach in  $Q^2$  to tackle some of the most fundamental and topical questions in hadronic physics.

We propose to measure  $G_E^n/G_M^n$  to high precision at  $Q^2 = 1.5 - 6.0 (\text{GeV}/c)^2$ , by quasi-elastic  ${}^2\text{H}(\vec{e}, \vec{e}' \vec{n})$ . This will provide an independent measurement to E02-013 [10] and overlap in kinematic range with the new experiment E12-09-016 [6], both of which employ  ${}^3\text{H}e(\vec{e}, n)$ . Existing  ${}^2\text{H}(\vec{e}, \vec{e}' \vec{n})$  data [11] extend up to  $Q^2 = 1.5 (\text{GeV}/c)^2$ .

Neutron measurements are technically very challenging and must employ quasi-free scattering from nuclei, which introduces some uncertainty in extrapolation to the free-neutron case. Thus it is important to have different experimental techniques, with different systematic effects, and different nuclear targets, with different binding and final state interaction effects. The present measurement will offer significantly improved precision of  $G_E^n/G_M^n$ , compared to E12-09-016, in the several  $(\text{GeV}/c)^2$  domain. However, it will not be possible to reach as high values of  $Q^2$  as E12-09-016 as the efficiency of the recoil-polarimetry technique becomes too low at neutron momenta  $\gtrsim 5 \text{ GeV}/c$ .

## 1.1 Physics Motivation

The study of the electromagnetic form factors remains central to the progress that is being made in understanding hadron structure, as attested by the huge number of citations of the JLab  $G_E^p/G_M^p$  measurements [12]. Several theoretical approaches, which are outlined in the following subsections, have been taken to calculate the elastic form factors.

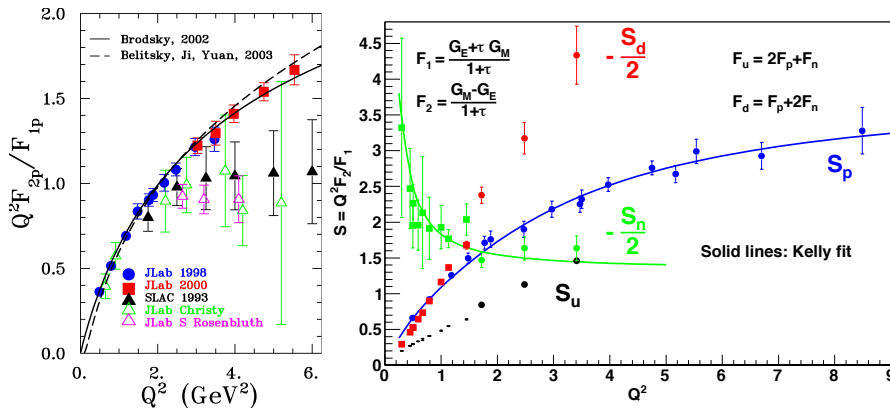


Figure 2:  $Q^2 F_2/F_1$  as a function of  $Q^2$ . Left: proton data derived from world double polarized measurements (red, blue) and Rosenbluth separation (green, magenta, black) compared to the theoretical predictions of Ref.[20]. Right: the fit of [22] to proton (blue) and neutron (green) world data. Also shown is a flavor decomposition with  $u$  (black) and  $d$  (red).

### 1.1.1 pQCD Scaling and Scaling Violations

The Sachs form factors  $G_E, G_M$  are linear combinations (Eq.4) of the fundamental Dirac ( $F_1$  helicity conserving) and Pauli ( $F_2$  helicity flip) form factors. At sufficiently high values of  $Q^2$ ,  $F_1$  should scale as  $1/Q^4$ , while  $F_2$  should scale as  $1/Q^6$  [13], essentially on the basis of quark counting rules. After Ref.[12], it became clear that the proton  $F_2/F_1$  did not scale as  $1/Q^2$ , as evident in Fig.2. The difference in apparent scaling behavior of proton data derived from double-polarized measurements [14, 15, 16], as opposed to Rosenbluth separation of differential cross sections [17, 18, 19], is discussed in Sec.2. The apparent scaling behavior of data obtained by Rosenbluth separation is now thought to be spurious.

A more recent pQCD calculation [20] relaxed the assumption [13] that the quarks move collinearly with the proton. It included components in the light-cone nucleon wave functions with a quark orbital angular momentum projection  $L_z = 1$ . This is equivalent to relaxing hadron helicity conservation and produces the scaling relation  $F_2/F_1 \propto \ln^2(Q^2/\Lambda^2)/Q^2$ , where  $\Lambda$  is a non-perturbative mass scale.

Agreement with the JLab double polarized  $G_E^p/G_M^p$  measurements is quite good up to about 6 (GeV/c)<sup>2</sup> (Fig.4) although newer data, at higher  $Q^2$ , suggest a more gradual fall off with  $Q^2$ . The implication of this scaling is that quark orbital angular momentum is playing an important dynamical role in the  $Q^2$ -evolution of the proton form factors. At sufficiently high values of  $Q^2$  one still expects that  $F_1/F_2$  will scale as  $1/Q^2$ , but observation of the transition to this behavior is beyond the reach of current experimental facilities. Fig.2 (left) [21] displays both proton and neutron results from JLab, along with an empirical fit to the data [22].

With measurements of all four Sachs form factors, a flavor separation into the Dirac and Pauli form factors of the  $u$  and  $d$  quarks:  $F_{1,2}^u, F_{1,2}^d$  can be made.

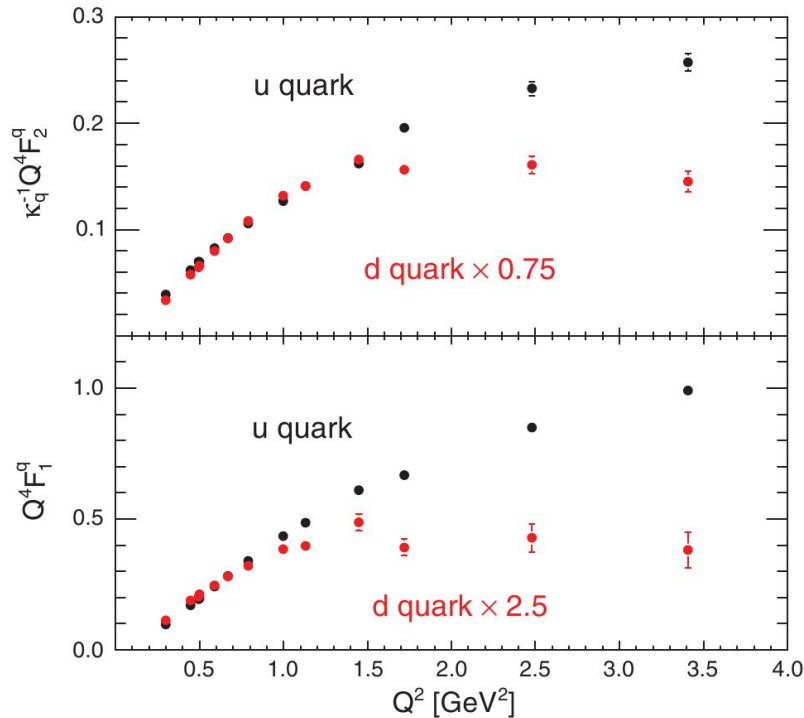


Figure 3: Left: Scaling behavior of  $u$  and  $d$  quarks from Ref. [1]. Right: cartoon of electron scattering from nucleon in di-quark configuration.

Assuming negligible nucleon strange content they are linear combinations of the proton and neutron form factors:

$$F_{1,2}^u(Q^2) = F_{1,2}^n + 2F_{1,2}^p \quad F_{1,2}^d(Q^2) = 2F_{1,2}^n + F_{1,2}^p \quad (1)$$

This emphasizes the importance of measuring both proton and neutron distributions, a major strength of the Hall-A SBS program. Although the nucleon data seem to be converging towards scaling behavior, there is little hint of this in the flavor-separated distributions. This work has been published recently [1] and shows an intriguing difference in scaling behavior between the  $u$  and  $d$  quarks. Above  $\sim 1$  (GeV/c) $^2$ ,  $F_{1,2}^d$  appears to scale roughly as  $1/Q^4$ , whereas  $F_{1,2}^u$  appears to scale roughly as  $1/Q^2$ .

This behavior is possibly suggestive of a significant di-quark configuration in the nucleon and certainly di-quark configurations are included in calculations using Dyson-Swinger formalism (Sec. 1.1.2). In addition the divergence in  $u - d$  scaling behavior is in qualitative agreement with the moments of GPD calculations (Sec. 1.1.2).

The analysis in Ref. [1] is certainly suggestive, but more data is needed to confirm the  $u - d$  form factor scaling behavior, from  $\sim 1.5$  (GeV/c) $^2$  to as high in  $Q^2$  as is feasible experimentally. The least well known of the four Sachs form

factors is  $G_E^n$ , where improvements in the precision and kinematic reach will have a large impact on future flavor-separation analyses.

### 1.1.2 Dyson-Schwinger Equation Calculations

This technique is based on the infinite series of Dyson-Schwinger Equations (DSE) that interrelate the Green's functions of field theories [23]. It has the potential to provide solutions to QCD in the non-perturbative regime with arbitrarily high accuracy. However, in any practical calculation the series of DSE must be truncated, and some Ansätze must be employed to account for the omissions. Recent calculations explicitly describe the dynamical generation of the mass of constituent quarks, and show excellent agreement with lattice QCD results that necessarily assume large current-quark masses.

Using dressed quarks as the elementary degrees of freedom, the nucleon form factors may be calculated using a Poincaré covariant Faddeev equation [24]. This work also assumes that two of the quarks couple into a di-quark. While still an approximation, the DSE/Faddeev approach is based on first principles. It is limited, however, in that precisely three constituent quarks are considered, so that for instance pion-cloud effects cannot be investigated. However, it is reasonable to assume the dominance of the 3-quark component of the wave function at relatively high values of  $Q^2$ .

DSE/Faddeev calculations have been made for many hadronic observables, including the Sachs form factors (Fig.4). The calculation of  $\mu_n G_E^n/G_M^n$  is consistent with the available data, but measurements at higher  $Q^2$  are required to test the predicted downturn in the ratio above  $Q^2 \sim 4.5$  (GeV/c)<sup>2</sup>. A recent DSE calculation of  $\mu_p G_E^p/G_M^p$  [25] is reasonably consistent with the data at higher  $Q^2$  and here the crucial question is the location of the zero crossing point (if any) of the ratio. This has implications for the location and width of the transition region between the non-perturbative and perturbative domains of QCD [25].

At moderate values of  $Q^2$  high precision measurements are well suited to investigate structural effects such as the di-quark. However, the extraction of meaningful structure information will require  $\sim 5\%$  experimental uncertainty. This proposal aims to make measurements of this quality.

### 1.1.3 Constituent Quark Models

Constituent Quark Models (CQM) have a long history of interpretation of the form-factor measurements that have come out of JLab. Even before the first JLab measurement of  $G_E^p/G_M^p$  [12], a relativistic CQM [26] predicted a strong decrease of  $G_E^p/G_M^p$  with  $Q^2$ . Subsequently it was shown [27] that the decrease of  $G_E/G_M$  is associated with a violation of helicity conservation, or equivalently non zero quark orbital angular momentum, which arises naturally from the relativistic treatment. Further work [28], using the so-called "light-front cloudy bag model", reproduced much of the form-factor data over a broad range of  $Q^2$ .

A limitation that is inherent to CQM calculations is that they do not respect the chiral symmetry of the QCD Lagrangian. The "cloudy bag model" is an early example of a bag model that restores chiral symmetry. The breaking of chiral symmetry gives rise to the pions, so by including them it is possible to restore

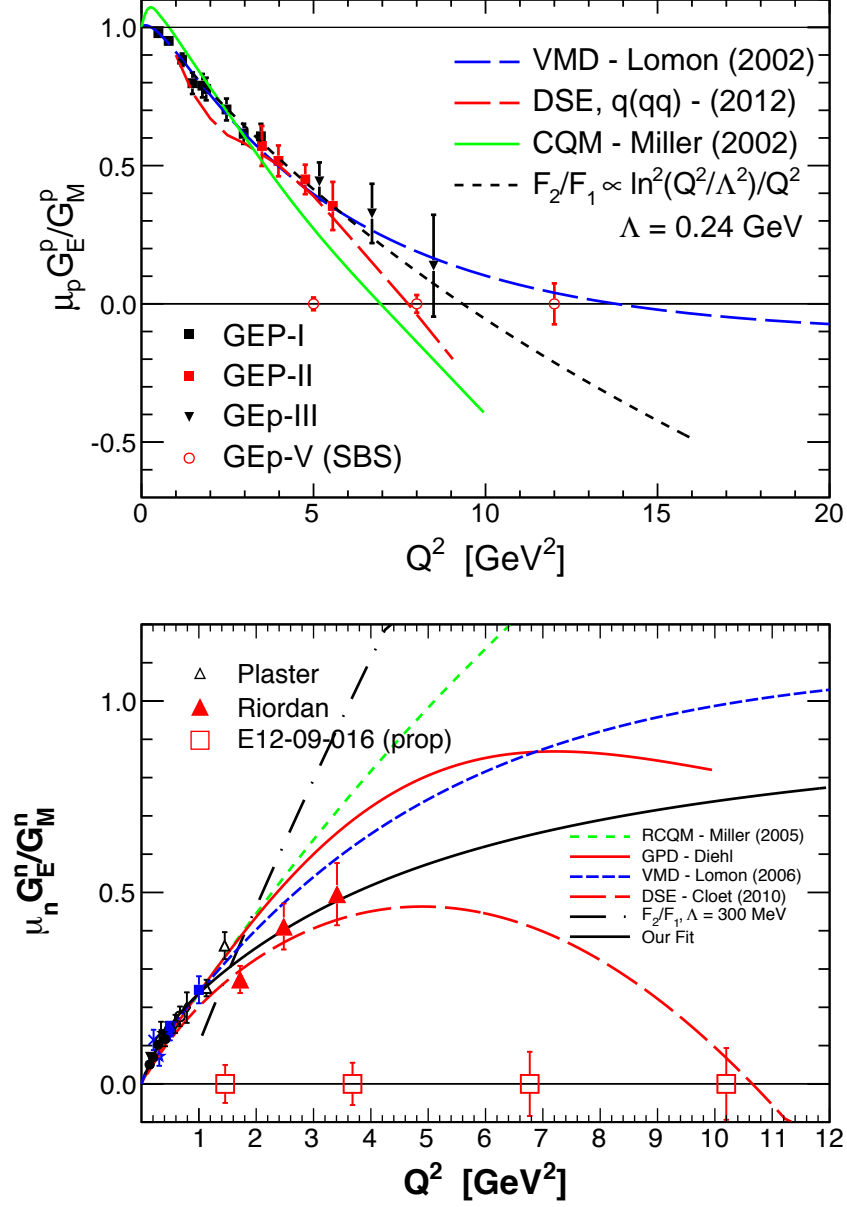


Figure 4: Form factor ratios  $G_E^n/G_M^n$  (right). On the top plot are shown the published  $G_E^p/G_M^p$  JLab results [14, 15, 16] and the projected results of GEp(5) [8]. On the bottom plot are shown previously published  $G_E^n/G_M^n$  data [11], the results of GEN(1) [10] and the projected uncertainties of GEN(2) [6]. The theoretical curves are as follows: VMD (blue dash) [44, 45]; RCQM (proton, green) [28]; RCQM (neutron, green dash) [30]; DSE (proton, red dash) [25]; DSE (neutron, red dash) [24]; GPD (neutron, red) [31].

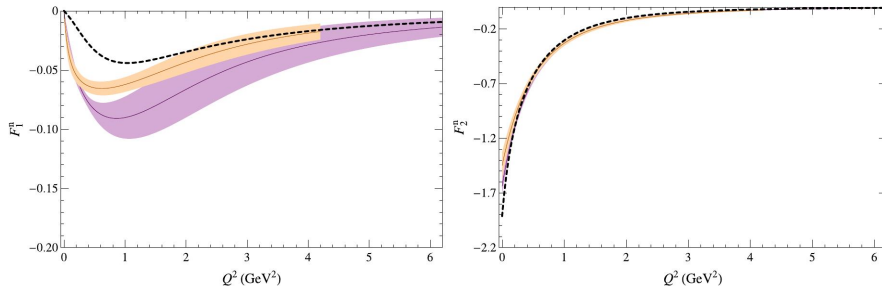


Figure 5: LQCD calculation [33] of neutron Dirac  $F_1$  and Pauli  $F_2$  form factors. The quenched approximation is shown in purple while dynamical calculations are in pink. The purple/pink shaded areas indicate the uncertainties in the calculation. The dashed line is derived from a fit [22] to the experimental data.

the symmetry of the theory. Inclusion of pions then leads to a pion cloud, which in turn governs certain aspects of the the low- $Q^2$  behavior of the form factor. Thus precise form factor measurements in this kinematic domain have immense potential to illuminate such fundamental structure phenomena.

With the interpretation of an appropriate model that respects both Poincaré invariance and chiral symmetry, the importance of both quark orbital angular momentum and the pion cloud is emphasized. The light-front cloudy bag model is in quite good agreement (Fig.4) with the double-polarized  $G_E^p/G_M^p$  data, although the newest data suggests a slower drop with  $Q^2$ . The  $G_E^n/G_M^n$  calculation seems to rise rather faster with  $Q^2$  than the data, although the slope suggested by the data is not entirely unambiguous.

#### 1.1.4 Lattice QCD

A true *ab initio* approach to calculate the properties of hadrons is based on discretizing space-time into a four-dimensional lattice with a fixed lattice spacing and volume.

There have been several on-going calculations of form factors (e.g. [32]) using Lattice QCD (LQCD), but typically they have been limited to  $Q^2 \lesssim 2.5$  (GeV/c) $^2$ , due to worsening computational signal-to-noise ratio. Fig. 5 displays recent calculations [33] of neutron Dirac and Pauli form factors, which extend out to  $Q^2 \lesssim 6$  (GeV/c) $^2$  (in the case of the quenched approximation) and compares them with a fit to the experimental neutron form factor data [22].

Differences in  $F_1$  between quenched and dynamical studies indicate systematic error due to quenching, while  $F_2$  appears less sensitive to sea-fermion effects. Due to the omission of “disconnected” diagrams,  $F_1^n$  and  $G_E^n$  have relatively large systematic errors at moderate momentum transfer, and accurate  $G_E^n$  data in the few-(GeV/c) $^2$  domain is certainly required to guide the LQCD effort. Presently a major impediment to reaching higher  $Q^2$  is the granularity of the available lattices, but this situation will certainly improve with increasing computational power.

The interplay between LQCD calculations, other calculation techniques and experiment can be very powerful. While LQCD calculations of form factors

clearly have a way to go, they are already providing serious predictions that are in reasonable agreement with experiment. They can also, for instance, be compared with non-lattice calculations in which the physical content of the theory is more readily evident. When lattice calculations, non-lattice calculations, and experiment are all found to agree, considerable insight can be gained.

### 1.1.5 Generalized Parton Distributions

Generalized Parton Distributions (GPD) [34, 35] describe correlations between spatial and momentum degrees of freedom and permit the construction of various types of “3-D images” of the nucleon. An example of a particularly powerful result to come out of the GPD framework is the “Ji Sum Rule”, which relates the total angular momentum of the quarks to sums over some of the GPDs. The Ji Sum Rule provides an important key to understanding the origin of the spin of the nucleon.

Knowledge of the nucleon elastic form factors is critical to the experimental determination of GPDs, since their first moments are related to the elastic form factors through model independent sum rules:

$$\int_{-1}^{+1} dx H^q(x, \xi, Q^2) = F_1^q(Q^2) \quad \int_{-1}^{+1} dx E^q(x, \xi, Q^2) = F_2^q(Q^2) \quad (2)$$

These relations are currently some of the most important constraints on the forms of the GPD’s and, since it is extremely unlikely that the GPDs will be mapped out exhaustively in the near future, constraints such as those in Eq.2 will be critical to their practical determination. Already the constraints from Eq.2 have played an important role in the first estimates of nucleon quark angular momentum using the Ji Sum Rule and constraining GPDs is in itself an excellent reason to experimentally determine the nucleon elastic form factors.

A GPD based derivation of  $G_E^n/G_M^n$  is compared to the data in Fig.4. It is apparently consistent with the data, although the data are somewhat ambiguous around  $1.5 \text{ (GeV/c)}^2$ .

### 1.1.6 Quark Orbital Angular Momentum

The role of quark orbital angular momentum (qOAM) in the internal dynamics is a common thread in virtually all of the theoretical explanations of the  $Q^2$ -dependence of  $G_E^p/G_M^p$ . Evidence for qOAM also comes from other sources.

The DIS spin asymmetry  $A_1^n$  for the neutron [36] has been measured at high values of Bjorken  $x$  and compared with both relativistic CQM and pQCD predictions. The measured value of  $A_1^n$  was in disagreement with the pQCD prediction, which assumed hadron helicity conservation, but in reasonable agreement with the CQM calculations where qOAM has dynamical importance.

Single-spin (target) asymmetries in Semi Inclusive DIS (SIDIS) have been measured at HERMES [37], COMPASS [38] and recently at JLab [39, 40]. The interpretation of these asymmetries in terms of the Sivers mechanism is helping to illuminate the dynamical role for qOAM. From SPIN RHIC [43] the contribution of gluon spin  $\Delta G$  to the nucleon spin is small, although the constraints

on  $\Delta G$  are not particularly stringent. The main message coming from all of this work is that we have a poor understanding of the spin of the nucleon. Polarized DIS results suggest that only 20-30% of the composite spin is due to the spin of the quarks and it is certainly possible that some of the remaining spin is due to qOAM. As such, polarized SIDIS measurements will continue to be an important part of the Hall-A experimental program post upgrade [41, 42].

### 1.1.7 The Form Factors as a Hadronic Model Testing Ground

Fig.4, shows existing data for  $G_E^p/G_M^p$  and  $G_E^n/G_M^n$ , the projected errors for approved new experiments, and the results of several theoretical calculations, outlined in the previous subsection. The approved experiments associated with the SBS program are E12-07-109 (also known as GEp(5)), and E12-09-016 (also known as GEn(2)), which will measure  $G_E^p/G_M^p$  and  $G_E^n/G_M^n$  respectively. Fig.4, makes it clear that the only way to achieve clarity in discriminating between theoretical explanations of the  $G_E/G_M$  data is to measure the form factors with high precision to high values of  $Q^2$ , for both the proton and the neutron. For example three of the predictions shown, the relativistic constituent quark model [27, 28], the DSE/Faddeev calculations [24, 25] and the refined pQCD calculation [20], all show  $G_E^p/G_M^p$  crossing zero somewhere in the neighborhood of 10  $(\text{GeV}/c)^2$ . In contrast, the two Vector Meson Dominance (VMD) models show  $G_E^p/G_M^p$  approaching zero much more gradually [44, 45, 46].

Considering the neutron, even by  $\sim 4$   $(\text{GeV}/c)^2$  the RCQM, pQCD and DSE/Faddeev calculations all differ markedly from one another. In the years following the discovery of [12] it is not surprising that models have evolved to explain the existing proton data. It is also not surprising that these models diverge strongly where there is little or no data to constrain the calculations. This applies at higher  $Q^2$  for the proton and down to moderate  $Q^2$  for the neutron. In general, higher values of  $Q^2$  also offer some theoretical simplifications that are not valid in a softer regime. For instance, the role of vector mesons is suppressed at higher  $Q^2$ , as are higher Fock states in some of the phenomenological models. Thus there are generally fewer places to hide deficiencies in a model.

The data for  $G_E^p/G_M^p$  are approximately linear with  $Q^2$  up to  $\sim 6$   $(\text{GeV}/c)^2$ , but the results from GEp(3) [16], up to values  $\sim 8.6$   $(\text{GeV}/c)^2$ , suggest a flattening of the gradient. By going to 14.5  $(\text{GeV}/c)^2$  the trend of  $G_E^p/G_M^p$  should become clear, but only if the data have sufficient precision. The projected errors for GEp(5), which is based on SBS, present a challenge to theory out to 14.5  $(\text{GeV}/c)^2$ , since the SBS approach provides a factor of 10 improvement in the polarimeter Figure-of-Merit. Eventually (from pQCD)  $G_E^p/G_M^p$  should level off and become constant. Evidence of a transition to this behavior would provide valuable insight and it is important to have an experiments capable of achieving high precision at high  $Q^2$ .

With respect to the neutron, the measurement of  $G_E^n/G_M^n$  out to  $Q^2 = 10$   $(\text{GeV}/c)^2$  has tremendous potential to assess various nucleon structure models. However, the various predictions for the neutron all start to diverge strongly above 3  $(\text{GeV}/c)^2$ . Further high-precision measurements in this region, using a different experimental technique, are required to confirm the GEn(1) results [10] and the previous Hall-C recoil polarimetry results [11]. Where the two data sets meet around 1.5  $(\text{GeV}/c)^2$  there is an interesting possible discrepancy, although

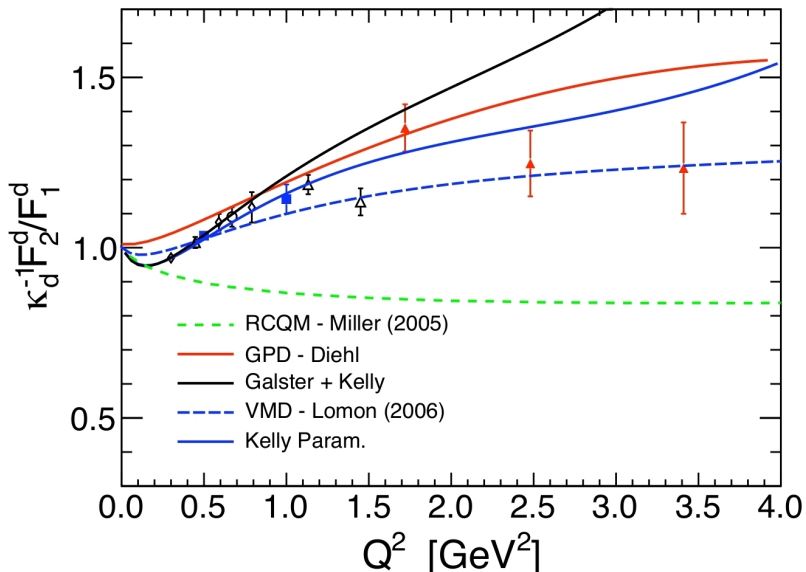


Figure 6:  $Q^2$  dependence of separated  $d$  quark ratio  $\kappa_d^{-1} F_2^d / F_1^d$ .

the significance is marginal. This emphasizes the need for high-precision, accurate neutron data in providing unambiguous guidance to theory. Measurement to high  $Q^2$  is vital, but it is no less important to have top-quality data at moderate  $Q^2$ . Theoretical divergence is less pronounced in this region, but it is possible to achieve much better precision at moderate  $Q^2$  and achieve low systematic uncertainties in a  ${}^2\text{H}(\bar{e}, e' \bar{n})$  measurement. Moderate  $Q^2$  is also optimum to illuminate longer-range structure effects.

Fig.6 displays the separated  $d$  quark ratio  $F_2^d / F_1^d$ , which requires both proton and neutron data. It is evident that the current level of experimental precision needs to be improved to provide unambiguous theoretical guidance.

## 2 Observables and Previous Experiments to Access the Form Factors

The present experiment will be part of a program in Hall-A to measure the 4 nucleon Sachs form factors to multi- $(\text{GeV}/c)^2$  values of  $Q^2$ . With sufficient precision and accuracy, these will provide a severe challenge to existing, QCD-inspired models of the nucleon and eventually to LQCD calculations.

In the one-photon exchange approximation the most general form of a relativistically covariant hadronic current for a spin-1/2 nucleon, which satisfies current conservation, is:

$$J_{hadronic}^\mu = e\bar{N}(p') \left[ \gamma^\mu F_1(Q^2) + \frac{i\sigma^{\mu\nu}q_\nu}{2M} F_2(Q^2) \right] \quad (3)$$

where  $\bar{N}(p')$  is the nucleon Dirac spinor for the final momentum  $p'$ , and  $F_1(Q^2)$  and  $F_2(Q^2)$  are the Dirac (helicity conserving) and Pauli (helicity flip) form factors. It is often convenient to express cross sections and other measurable quantities in terms of the Sachs electric and magnetic form factors which are linear combinations of  $F_1$  and  $F_2$ .

$$G_E = F_1 - \tau F_2 \quad G_M = F_1 + F_2 \quad (4)$$

where  $\tau = Q^2/4M_N^2$ . A brief review of experimental techniques to access the form factors is presented below.

## 2.1 Rosenbluth Separation

The Sachs electric ( $G_E$ ) and magnetic ( $G_M$ ) form factors represent, in the Breit frame, the Fourier transforms of the distributions of charge and magnetic moment respectively of the nucleon constituents. As measured in elastic electron scattering, they are functions of  $Q^2$ , the squared four-momentum transfer, and may be extracted from the differential cross section, which can be cast in the form:

$$\sigma(\theta) = \sigma_M(\theta) \left\{ \left[ \frac{G_E^2(Q^2) + \tau G_M^2(Q^2)}{1 + \tau} \right] + 2\tau G_M^2(Q^2) \tan^2 \frac{\theta_e}{2} \right\} \quad (5)$$

$$\sigma_M = \frac{\alpha^2 \cos \frac{\theta_e}{2}}{4E_e^2 \sin^4 \frac{\theta_e}{2}} \cdot \frac{E'_e}{E_e}$$

where  $\sigma_M$  is the Mott cross section (with recoil correction) for scattering from a point object,  $\theta_e$  is the electron scattering angle and  $\tau = Q^2/4M_N$ . The Rosenbluth technique to separate electric and magnetic components entails measurement at different combinations of electron beam energy and scattering angle, such that  $Q^2$  is held constant. After Hofstadter performed pioneering measurements in the 1950's [2], the precision improved and kinematic range extended. In the case of the proton, for relatively low momentum transfer, Rosenbluth separation seems to work reasonably well. However, for  $G_E^n$  and  $G_E^p$  at high  $Q^2$ , where  $G_E \ll G_M$  and the factor  $\tau$  is increasing, it is extremely difficult to determine  $G_E$  with any reasonable degree of precision or accuracy. Rosenbluth is a demanding technique requiring extreme care in accounting for changes in detector acceptance, among other things.

Another more subtle issue has emerged in recent years. The validity of Eq.5 depends on the one-photon-exchange or Born approximation. It has now been established that two-photon contributions to the cross section, at higher values of  $Q^2$ , are sufficiently large that the separation of the form factors has been severely compromised. This makes the determination of electric form factors by alternative techniques vital. The difference between  $G_E^p/G_M^p$  measurements taken using a double-polarized technique or Rosenbluth separation is illustrated in Fig.1.1.1.

## 2.2 Double polarized measurements

The double polarization method for the measurement of  $G_E$  was originally proposed [47] to improve the experimental sensitivity to the spin-flip form factor  $F_2$  at large momentum transfer, and subsequent work [48] developed the formalism. However, the experimental realization of these techniques had to wait for high-intensity, high-duty-factor accelerators, capable of delivering polarized electron beams. A number of form-factor measurements have been performed in recent years, using two versions of the double-polarization method: either with polarized nucleon targets, or with a polarimeter to measure the polarization transfer to the recoiling nucleon. The technique of choice depends on the comparison of achievable luminosity, detector efficiency, detector acceptance and the experimental asymmetry, which in turn depends on the target polarization or polarimeter analyzing power.

In the case of the neutron there is no free target and quasi-elastic scattering from the neutron embedded in  $^2\text{H}$  or  $^3\text{He}$  offers the nearest practical approximation to the free case. Bound-nucleon and final-state-interaction effects become less important as momentum transfer increases, but none the less it is highly desirable to have data on both targets to check consistency. Neutron measurements are inherently more challenging than their proton equivalents, as demonstrated by their more restricted kinematic range  $G_E^n/G_M^n : Q^2 \leq 3.5 \text{ (GeV/c)}^2$  as opposed to  $G_E^p/G_M^p : Q^2 \leq 8.5 \text{ (GeV/c)}^2$ . A set of high precision measurements of  $G_E^n/G_M^n$  at  $Q^2 = 1.5 - 6 \text{ (GeV/c)}^2$  will have extremely high selectivity of the quite diverse predictions of different theoretical models. Thus it is extremely important to have reliable, independently verified neutron results.

Whether working with a polarized target or a recoil polarimeter, the ability separate  $G_E$  from the much larger  $G_M$  and the relative freedom from two-photon exchange effects make double-polarization asymmetry measurements the techniques of choice for measuring  $G_E^n$ .

### 2.2.1 Polarized Beam and Polarized Target

The asymmetry may be expressed as

$$A = A_{\perp} \sin \theta \cos \phi + A_{\parallel} \cos \theta = \frac{a G_E/G_M \sin \theta \cos \phi}{(G_E/G_M)^2 + c} + \frac{b \cos \theta}{(G_E/G_M)^2 + c} \quad (6)$$

where  $a = -2\sqrt{\tau(1+\tau)} \tan(\theta_e/2)$ ,  $b = 2\sqrt{\tau [1 + (1+\tau) \tan^2(\theta_e/2)]}$ ,

$c = \tau [1 + 2(1+\tau) \sin^2 \tan^2(\theta_e/2)]$ ,  $\phi'$  is the angle between the nucleon and electron scattering planes and  $\theta'$  is the angle the the nucleon polarization makes with  $\vec{q}$ . Where  $\phi' \sim 0,180$  and  $\theta' \sim 90$ ,  $A \propto G_E/G_M$ .

The projected errors for the new GEn(2) experiment (Fig.4) are roughly 20% for data points on the often cited Galster parameterization. The three GEn(1) data points, currently the highest-value  $Q^2$  points in existence, have uncertainties  $\sim 15\%$ . While it is clear that, in terms of precision, polarized target experiments are better at  $Q^2 \sim 10 \text{ (GeV/c)}^2$ , recoil polarimetry is highly competitive at  $Q^2 \lesssim 6 \text{ (GeV/c)}^2$ .

### 2.2.2 Polarized Beam and Recoil Polarimetry

In the case of a free nucleon, assuming the one-photon exchange approximation, the polarization transferred from the electron to the nucleon can be written as:

$$P_x = -hP_e \frac{2\sqrt{\tau(1+\tau)} \tan \frac{\theta_e}{2} G_E G_M}{G_E^2 + \tau G_M^2 (1 + 2(1+\tau) \tan^2 \frac{\theta_e}{2})} \quad (7)$$

$$P_y = 0 \quad (8)$$

$$P_z = hP_e \frac{2\tau \sqrt{1+\tau + (1+\tau)^2 \tan^2 \frac{\theta_e}{2}} \tan \frac{\theta_e}{2} G_M^2}{G_E^2 + \tau G_M^2 (1 + 2(1+\tau) \tan^2 \frac{\theta_e}{2})} \quad (9)$$

$$\frac{P_x}{P_z} = \frac{1}{\sqrt{\tau + \tau(1+\tau) \tan^2 \frac{\theta_e}{2}}} \cdot \frac{G_E}{G_M} \quad (10)$$

where  $h$  and  $P_e$  are the helicity and polarization respectively of the electron beam. Thus the ratio  $P_x/P_z \propto G_E/G_M$  and  $G_M$  may be obtained from the differential cross section (Eq.5). In the case of the neutron, a free-nucleon target is not feasible and here one must use quasi-elastic scattering from the neutron embedded in a nucleus. The deuteron is an obvious choice as the  $p-n$  system is bound weakly, so that quasi-free scattering is a good approximation to the free case at incident momenta  $\gtrsim 1$  GeV. In addition, the handling of the  $p-n$  final state is considerably simpler than the case of  $p-p-n$  from a  ${}^3\text{He}$  target. Eq.10 requires the measurement of the longitudinal component of the neutron polarization and this must be precessed into the transverse plane. The angle of precession through a magnetic field may be expressed as

$$\chi = \frac{2\mu_n}{\hbar c} \frac{1}{\beta_n} \int_L \mathbf{B} \cdot d\mathbf{l} \quad (11)$$

where  $L(x, y, z)$  is the path through the field,  $\mathbf{B} = (B_x, B_y, B_z)$  is the flux density,  $\mu_n$  is the neutron magnetic moment and  $\beta_n$  is the neutron velocity. With a horizontal field  $(B_x, 0, 0)$  the spin will precess in the  $y-z$  plane (See Sec.2.3).

### 2.3 Nucleon Polarimetry

Nucleon polarimetry depends on the spin-orbit interaction of an incident nucleon with a target nucleon or nucleus, which produces an azimuthal modulation of the scattering process:

$$\sigma(\theta'_n, \phi'_n) = \sigma(\theta'_n) \left[ 1 + A_y^{eff}(\theta'_n) \left\{ P_x^n \sin \phi'_n + P_y^n \cos \phi'_n \right\} \right] \quad (12)$$

where  $\sigma(\theta'_n)$  is the unpolarized differential cross section,  $A_y^{eff}(\theta'_n)$  is the effective analyzing power of the scattering process and  $P_x^n, P_y^n$  are respectively the horizontal and vertical components of the incident nucleon polarization. Scattering angles are defined in Fig.7. Note that there is no dependence on the longitudinal

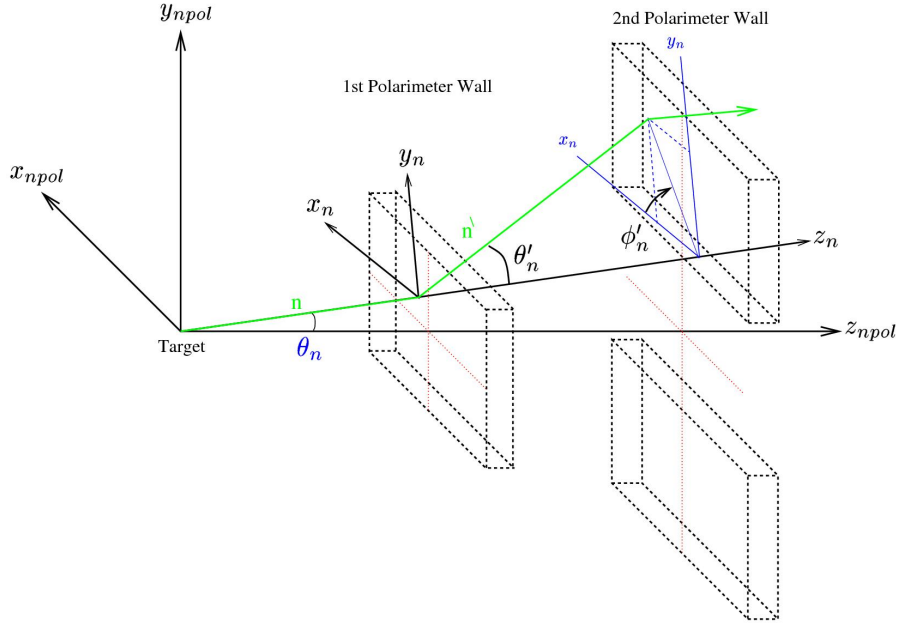


Figure 7: Schematic view of a typical neutron polarimeter. In this proposal incident neutrons would be directed along axis  $z_{npol}$ .

component  $P_z^n$ . A schematic representation of a typical polarimeter geometry is given in Fig.7. The effectiveness of any polarimeter will depend on its detection efficiency and the analyzing power, which can be parametrized as a figure of merit  $\mathcal{F}$  given by:

$$\mathcal{F}^2(p_n) = \int \varepsilon(p_n, \theta'_n) A_y^2(p_n, \theta'_n) d\theta_n \quad (13)$$

where  $\varepsilon(p_n, \theta'_n)$  is the detection efficiency which depends on the cross section for the scattering process, the thickness of the polarimeter material and the useful angular range covered. Obviously the angular range would be restricted to that where  $A_y$  is large. The thickness is usually limited in practice by multiple scattering considerations. If  $\mathcal{F}$  is known then the precision of the obtained incident polarization may be estimated as:

$$\Delta P = \sqrt{\frac{2}{N_{inc} \mathcal{F}^2}} \quad (14)$$

where  $N_{inc}$  is the number of incident particles. Note that the split rear wall depicted in Fig.7 is not always a desirable polarimeter feature. Full azimuthal coverage is preferable to untangle  $P_x$  and  $P_y$  polarization components and maximize acceptance. In the present project the rear detector will be a segmented hadron calorimeter, similar to that designed in Dubna [49] for the COMPASS experiment at CERN. With this detector, which will also be employed in experiment E12-07-108 [9], we will have full azimuthal coverage up to polar angles of

$\sim 15^\circ$ , which will contain most of the useful forward peaked scattering. Thresholds can be set high to suppress soft background so that the device can operate comfortably while open to the target.

## 2.4 Neutron Analyzing Power at Several GeV/c

In comparison to proton polarimetry, the analyzing power  $A_y$  for neutron polarimetry is rather poorly known. Elastic  $p-n$  scattering has been measured up to 11 GeV [50, 51] and  $A_y$  for both  $p-n$  and  $p-p$  have been parametrized [52] as a function of  $t$ . Quasi-elastic  $p-n$  scattering has also been measured at SATURNE [53] up to around 2.4 GeV and this data has been included in the SAID partial wave analysis [54] of nucleon-nucleon scattering data. While free  $n-p$  scattering remains in principle the best analyzer of neutron polarization, the use of a hydrogen analyzer is unfeasible technically. However, scattering from  $C$  or  $CH_2$  does offer a practical solution. For any neutron polarimeter with significant angular acceptance, the analyzer must be a position sensitive detector to allow the measurement of the initial and final directions of the neutron. Thus plastic scintillator ( $CH$ ) represents a suitable material.

In PR11-001 we proposed to measure the analyzing power for neutron scattering from plastic scintillator, using the polarized neutron beam at JINR Dubna. It now seems certain that polarized beams will not be available at the Dubna facility before the second half of 2013. Thus we have analyzed the available experimental evidence (Sec. 2.4.1) in order to obtain a present best estimate of the neutron analyzing power. In parallel we have commenced collaboration with the group of J. Udias in Madrid to perform theoretical calculations of  $n + {}^{12}C$  analyzing power at several GeV/c incident momentum.

### 2.4.1 Experimental Data

Information on polarized nucleon scattering in the domain  $p_N \gtrsim 2$  GeV/c has been obtained from two sources and is presented in Fig. 8.

1. Measurements of the asymmetries of the  $d(\vec{p}, p')n$  and  $d(\vec{p}, n)p$  processes were performed using the ZGS accelerator at ANL in the late 1970s [50, 51]. It is important to note that these experiments measured both  $p-p$  and  $p-n$  scattering. The  $d(\vec{p}, p')n$  measurements are consistent with elastic  $\vec{p} + p \rightarrow p + p$  measurements [55].
2. Inclusive measurements  $\vec{p} + CH_2 \rightarrow p + X$  [56], and  $\vec{p} + C \rightarrow p + X$  [57, 58] have been obtained in the calibration of proton polarimeters used at ANL, Dubna and JLab.

The maximum values of the  $t$ -dependent polarization asymmetries of  $p-p$  and  $p-n$  scattering were determined from Ref.[50, 51] and plotted in Fig.8 as a function of  $1/p_{lab}$ . Linear fits to these data give the result:

$$A_Y^{pp} = \mathbf{0.002} + 0.742/p_{lab} \quad A_Y^{pn} = \mathbf{-0.085} + 0.751/p_{lab} \quad (15)$$

While the  $p-p$  line is consistent with a (0,0) origin,  $p-n$  has a substantial negative offset, so that  $A_Y^{pn}$  crosses zero at  $(1/p_{lab}) = 0.114 \pm 0.012$ , i.e. at

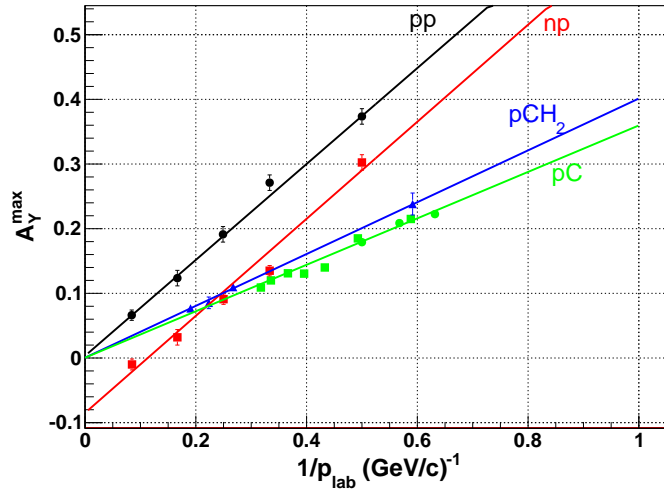


Figure 8: The dependence on inverse, incident proton momentum of the maximum of  $A_Y$ . For Ref. [50, 51]  $A_Y$  is the left-right scattering asymmetry, while for Ref. [57, 58, 56] it is the analyzing power of the proton polarimeter. Black circles: ANL  $d(\vec{p}, p')n$  data [50, 51]; black line: linear fit. Red squares: ANL  $d(\vec{p}, n)p$  data [50, 51]; red line: linear fit. Blue triangles [56]:  $\vec{p} + \text{CH}_2 \rightarrow \text{charged} + X$ ; blue line: linear fit [56]. Green squares [57] and circles [58]:  $\vec{p} + C \rightarrow \text{charged} + X$ ; green line: linear fit [56].

$p_{lab} = 8.8 \pm 1.0$  GeV/c. Most proton polarimeters employ C or CH<sub>2</sub> analyzers, where  $p - {}^{12}\text{C}$  interactions have a factor  $\sim 2$  reduction in analyzing power with respect to the free scattering case [57, 58, 56]. It is important to note that the linear fit of the maximum  $p - {}^{12}\text{C}$  analyzing power

$$A_Y^{pC} = 0.000 + 0.357/p_{lab} \quad (16)$$

extrapolates to zero at infinite  $p_{lab}$ , as with the free  $p - p$  case.

#### 2.4.2 The Analyzing Power of Neutron Polarimetry

Neutron polarimetry with plastic scintillator is based on  $n - p$  scattering processes, since the recoiling proton can induce a detectable signal in the analyzer. By contrast, quasi-free  $n - n$  scattering generally produces a recoiling charged ion with very low energy, which is not detectable.  $A_Y(\theta'_n)$  depends on the incident nucleon momentum and, for  $n - p$  scattering, the highest values occur at angle  $\theta'_n$ , which corresponds to a transverse momentum  $p_\perp = p_{lab} \sin \theta'_n \sim 400 - 500$  MeV/c. Thus, at the maximum incident momentum in this proposal ( $\sim 4$  GeV/c), the optimum neutron scattering angle is around  $7^\circ$ . Two methods are possible for measurement of  $\theta'_n$  (and  $\phi'_n$ ). The first detects the forward scattered neutron in the position-sensitive rear elements of the polarimeter. The second detects the track of the recoiling proton and reconstructs the neutron  $\theta'_n$  and  $\phi'_n$  assuming two-body kinematics.

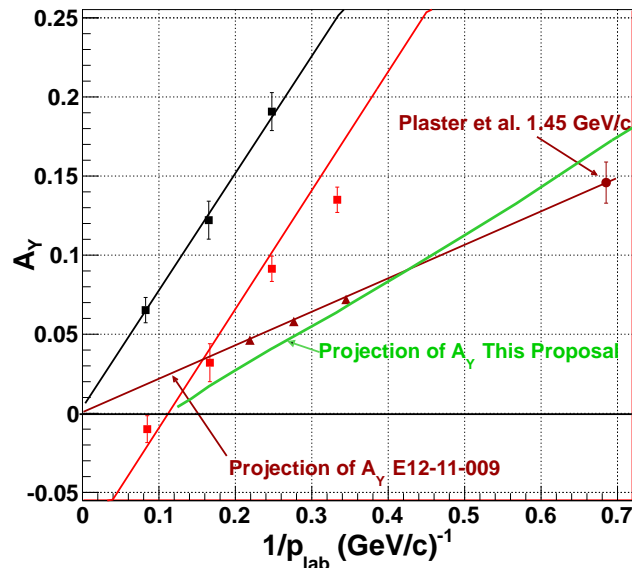


Figure 9: The analyzing power for neutron polarimetry. The black and red data points and lines are as in Fig.8. The brown line and points illustrate the analysis of  $A_Y$  given in E12-11-009 [59]. The green line shows our analysis, based on our fit (red line), to measurements of free  $p-n$  scattering data, which crosses zero at  $p_{lab} = 8.8$  GeV/c.

Most protons in CH material are bound in carbon and the bound proton effects on neutron analyzing power are large, as has been observed in proton polarimetry (Sec. 2.4.1). A previous JLab measurement of  $G_E^n/G_M^n$  [11] has yielded an estimate of neutron analyzing power  $A_Y^{mean} = 0.144$  at  $p_{lab} = 1.45$  GeV/c (Fig. 9), where  $A_Y^{mean}$  is the acceptance averaged analyzing power. The effect of acceptance averaging has been estimated as:

$$A_Y^{mean} = \frac{\int \sigma(\theta) A_Y(\theta) d\theta}{\int \sigma(\theta) d\theta} \quad (17)$$

where the integration was performed over the polar angle acceptance of the polarimeter, the scattering differential cross section  $\sigma(\theta)$  was taken from the SAID partial wave analysis and the angular dependence of  $A_Y$  was taken from Ref.[52]. The calculation yields  $A_Y^{mean} \sim A_Y^{max}/1.5$  for the polarimeter of Ref.[11]. Eq.15 gives  $A_Y^{max} = 0.42$  at  $p_{lab} = 1.45$  GeV/c for free  $n-p$  scattering. After taking the factor 1.5 for acceptance averaging into account (Eq.17), the free  $n-p$  scattering case is a factor  $\sim 2$  larger than the observation of Ref. [11], which is very similar to the proton polarimetry case (Sec. 2.4.1). We estimate that Fermi-motion smearing has a relatively small effect and the factor  $\sim 2$  presumably originates mainly from a spin-orbit interaction of the nucleon and nucleus.

In experiment E12-11-009 [59] the analyzing power of the polarimeter has been calculated by taking  $A_Y = 0.14$  at  $p_{lab} = 1.45$  GeV/c, assuming a linear dependence of  $A_Y$  on  $1/p_{lab}$  and extrapolating to  $A_Y = 0$  at infinite  $p_{lab}$  (brown

line and points Fig. 9). However, the assumption that  $A_Y$  extrapolates to zero at infinite momentum is plainly inconsistent with the published experimental data on free  $p - n$  scattering. Here we have taken  $A_Y^{max} = 0.5 \times A_Y^{pn}$  (Eq.15) for  $n - p$  scattering on bound protons and performed an acceptance average as in Eq.17. The average has been performed for scattering angles covering  $-t = 0.02 - 0.4$  (GeV/c)<sup>2</sup>, which is equivalent to  $p_{\perp} \sim 0.15 - 0.70$  GeV and consistent with the acceptance of the present polarimeter. This yields values of  $A_Y^{mean}$  falling on the green line of Fig. 9, which have been used (Table 6) in the estimates of precision given in Sec. 5.1.

## 2.5 Previous Form Factor Measurements and Proposals

### 2.5.1 Unpolarized

Recently a new Rosenbluth measurement of the proton form factor [19] at  $Q^2$  values of 2.64, 3.20 and 4.10 (GeV/c)<sup>2</sup> has been made in Hall-A. Differential cross sections were determined by detecting the recoiling proton, in contrast to previous measurements where the scattered electron was detected, and relative cross sections were claimed to better than 1%. The measurement focused on the extraction of  $G_E^p/G_M^p$  which was determined to 4-8% and found to follow form factor scaling, i.e.  $\mu G_E \sim G_M$ . These results (Fig.2) are consistent with, and much more precise than, previous Rosenbluth extractions. They are in definite disagreement with recent polarization transfer measurements of comparable precision, which may be attributed to the relative sensitivity of Rosenbluth separation to two-photon-exchange effects.

### 2.5.2 Polarized Target

Vector Polarized <sup>2</sup>H has the neutron and proton spins aligned in parallel and measurements with such a polarized neutron-proton target have been made at  $Q^2 = 0.21$  [60] and 0.495 (GeV/c)<sup>2</sup> [61]. Corrections for various effects amounted to  $\sim 13\%$  in [61], compared to  $\sim 8\%$  for a recoil polarimetry experiment [62] at slightly lower  $Q^2$ .

Polarized <sup>3</sup>He has the advantage that  $\sim 90\%$  of the nuclear polarization is carried by the neutron. At Mainz, polarized <sup>3</sup>He target measurements have taken place at  $Q^2 = 0.385$  (GeV/c)<sup>2</sup> [63] and 0.385 (GeV/c)<sup>2</sup> [64]. Subsequent measurements at 1.5 (GeV/c)<sup>2</sup> are not fully analyzed, but a preliminary data point [65] is consistent with GEn(1) measurements. In the GEn(1) experiment at JLab [10] the high beam energy, high performance <sup>3</sup>He target and large acceptance detectors has enabled the  $Q^2$  range to be stretched up to 3.4 (GeV/c)<sup>2</sup>.

The effective figure of merit of GEn(1) represents more than an order-of-magnitude improvement over previous experiments and already the results are providing valuable insight regarding the scaling of the form factors. In Ref.[20] the proton results were explained quite well by a logarithmic scaling, brought about by the introduction of non-zero quark orbital angular momentum. Application of this scaling to the neutron data is shown in the bottom plot of Fig.4 as a black dot-dash line. It is clearly well above the data points from GEn(1). The prediction of the "light front cloudy bag model" of Miller [28], which anticipated the scaling results of  $G_E^p/G_M^p$ , also appears to overestimate the slope of  $G_E^n/G_M^n$  with  $Q^2$ . It

is clear is that much can be learned by extending neutron measurements to yet higher values of  $Q^2$  and Hall-A experiment E12-09-016 [6], which will extend to  $10 \text{ (GeV/c)}^2$ , has been awarded 50 days of beam time.

### 2.5.3 Recoil Polarimetry

There have been several experiments to measure  $G_E^n/G_M^n$  by recoil polarimetry. Proof-of-principle measurements at MIT-Bates [66] were followed by more quantitative measurements at Mainz, firstly within collaboration A3 [62, 67] and subsequently within collaboration A1 [68]. While the Mainz program was still in progress, experiments at JLab started to come online, and Hall-C measurements of  $G_E^n/G_M^n$  have been published at  $Q^2$  of 0.5 and 1.0  $(\text{GeV/c})^2$  [69] and 1.45  $(\text{GeV/c})^2$  [11]. The beam energy at JLab is significantly higher than Mainz (currently 6.0 GeV, as opposed to 1.6 GeV) and in 2013 a high intensity 11 GeV beam will become available at JLab. The higher beam energy is obviously important to achieve the high  $Q^2$   $G_E^p/G_M^p$  data points of GEp(5), but for  $G_E^n/G_M^n$  measurements at somewhat lower  $Q^2$ , a lower beam energy gives superior kinematic conditions.

At JLab, experiment E12-11-009 using the  ${}^2\text{H}(\vec{e}, e' \vec{n})$  reaction has been proposed [59] for Hall-C up to  $Q^2 = 6.88 \text{ (GeV/c)}^2$ . The practice and interpretation of all  $G_E^n/G_M^n$  measurements is very challenging and independent verification of data should be mandatory. Thus we believe that a new  ${}^2\text{H}(\vec{e}, e' \vec{n})$  experiment is necessary and timely. However, our calculations show that the present experimental technique has a large advantage over E12-11-009 in terms of overall figure of merit, which is discussed in Sec.2.6.1.

## 2.6 New Elastic Form Factor Measurements at JLab.

Measurement of the nucleon elastic form factors will be a major theme in Hall-A after the CEBAF upgrade. The SBS project has three approved measurements:  $G_E^p/G_M^p$  [8],  $G_E^n/G_M^n$  [6], and  $G_M^n/G_M^p$  [7] by the cross section ratio method. These three measurements, together with a very precise measurement of  $G_M^p$  [9] in Hall A using the HRS Spectrometers (not part of the SBS Program), will collectively determine all four nucleon form factors with unprecedented reach in  $Q^2$  and accuracy. The figures of merit provided by the various SBS configurations represent an improvement of between 10 and 50 over all past and proposed experiments. Thus the achievable precision made possible by the SBS apparatus is second to none, and will provide a challenge to theory for many years to come. We briefly describe our experimental plan for each of the three proposed measurements.

1.  $G_E^p/G_M^p$  up to  $12 \text{ (GeV/c)}^2$  using Recoil Polarization.  
Experiment E12-07-109 or GEp(5), will measure the ratio  $G_E^p/G_M^p$  at  $Q^2 = 5, 8, 12 \text{ (GeV/c)}^2$ , close to doubling the maximum  $Q^2$ -value of GEp(3) while maintaining a relative uncertainty of  $\sim 0.1$  (Fig.4). The GEp(5) experiment will use the 11 GeV polarized electron beam, a 40 cm long liquid hydrogen target, and a customized detector system. An electromagnetic calorimeter, will detect the elastically scattered electrons. Originally the “BigCal” lead glass calorimeter was proposed, but now the collaboration

is considering an alternative device from DESY. SBS, equipped with a double polarimeter, will be used for the detection of the recoiling proton.

2. *Precision Measurement of the Neutron Magnetic Form Factor up to  $Q^2 = 13.5 \text{ (GeV/c)}^2$ .*

In experiment E12-09-019 the combination of high precision measurements of  $G_M^p$  and  $G_M^n$  will permit the reconstruction of the individual  $u$  and  $d$  quark distributions with an impact-parameter resolution of 0.05 fm. These data are needed both to determine the  $u-d$  difference and to study the QCD mechanisms which govern these distributions. Eventually it is hoped to reach as high as  $Q^2 \leq 18 \text{ (GeV/c)}^2$  in Hall-A [7], which will match the kinematic reach of the  $G_M^p$  experiment [9]. The magnetic form factor of the neutron has been measured accurately up to  $4.5 \text{ (GeV/c)}^2$  [70], but the existing data for higher  $Q^2$  [71] have uncertainties of about 10-20%. In E12-09-019 [7]  $G_M^n$  will be obtained from the cross-section ratio of  ${}^2\text{H}(e, e'n)$  and  ${}^2\text{H}(e, e'p)$  quasi-free scattering from the deuteron. This ratio method has also been proposed using CLAS12 [72], which can measure on a fine grid of  $Q^2$  points. However, the SBS measurement can be made at much higher luminosity and can achieve superior precision at high  $Q^2$ . The HCAL calorimeter for the SBS measurement offers very similar proton and neutron detection efficiencies which are close to 100%. This largely eliminates a potential major source of systematic uncertainty in the ratio method.

3.  $G_E^n/G_M^n$  up to  $Q^2 = 10 \text{ (GeV/c)}^2$ .

Experiment E12-09-016 [6] ( $\text{GEn}(2)$ ), will measure the double-spin asymmetry in quasi-elastic  ${}^3\text{He}(\vec{e}, e'n)\text{pp}$  using a new highly-polarized  ${}^3\text{He}$  target, capable of withstanding beam currents as high as  $65 \mu\text{A}$ . The scattered electron will be detected in BigBite which was also used successfully during  $\text{GEn}(1)$ . The BigBite detector stack will be upgraded to include a GEM tracking system and the recoiling neutron will be detected using a large segmented hadron calorimeter HCAL. HCAL will also be used in E12-07-109 and E12-09-019. For E12-09-016 the SBS dipole magnet will be located between the target and the neutron detector, to facilitate the separation of charged and neutral quasi-elastic events. The physics impact of  $\text{GEn}(2)$  is illustrated in Fig.4, which shows both existing and projected data. Measurements are proposed at  $Q^2 = 1.5, 3.7, 6.8, 10.2 \text{ (GeV/c)}^2$ , which can be compared to the current highest  $\text{GEn}(1)$  point at  $Q^2 = 3.4 \text{ (GeV/c)}^2$ . However, given that neutron measurements are extremely challenging, it is vital to have independent confirmation of the polarized target results. There is a hint (Fig.4: bottom plot) that recoil-polarimetry and polarized-target  $G_E^n/G_M^n$  measurements may not be entirely consistent at  $Q^2 \sim 1.5 \text{ (GeV/c)}^2$ . The present proposal to measure the range  $1.5 - 6.0 \text{ (GeV/c)}^2$  to high accuracy and precision has the potential to settle any possible ambiguities in the current data set.

### 2.6.1 Comparison of the Present Proposal to Hall-C Experiment E12-11-009

A measurement of  $G_E^n/G_M^n$  by recoil polarimetry has been proposed [59] for Hall-C using the Super High Momentum Spectrometer (SHMS) and a custom built polarimeter. We believe that the apparatus described in this proposal offers many advantages over E12-11-009.

**The Electron Detectors** Compared to the SHMS, BigBite offers a much larger angular acceptance on the electron arm, which is well matched to the acceptance of the neutron-arm polarimeter. The large acceptance is vital to achieve good counting statistics in a reasonable time. Good statistics can be achieved using a luminosity which produces reasonable counting rates in both electron and neutron arms of the experiment.

**The Polarimeters** The present neutron polarimeter (Pol-A) and the polarimeter of E12-11-109 (Pol-C) both use plastic scintillator analyzers, but differ in several important respects.

In Pol-A the  $n - p$  scattering interaction is registered in a highly segmented analyzer array of plastic scintillators. This provides the primary interaction coordinate. Scattered neutrons are detected in a segmented Fe-plastic calorimeter, which registers neutrons with high efficiency and good coordinate resolution. It can suppress low energy background extremely effectively and can operate in direct view of the target. Pol-A covers  $\theta'_n$  (Eq. 12) in the range  $\sim 2 - 15^\circ$  and  $\phi'$  over the full  $360^\circ$  (Sec.2.4.2). Thus the full azimuthal dependence of the scattering asymmetry may be analyzed. Good scattering-angle resolution of  $0.7^\circ$  allows offline selection of  $\theta'_n$  for maximum values of  $A_Y$ , to optimize the polarimeter FoM. The overall efficiency of Pol-A, after selection of scattering angle to optimize  $A_Y$ , will be  $\sim 7\%$ , with no significant incident momentum dependence. The Pol-C efficiency varies from 4 - 5.9% as the incident neutron momentum increases from 2.9 - 4.5 GeV/c.

Pol-C registers  $n - p$  interactions in a series of segmented plastic-scintillator analyzers and detects recoiling protons in top and bottom, segmented arrays of  $\delta E - E$  counters. Recoiling proton momenta below 310 MeV/c are not detected and this leads to a significant loss of polarimeter FoM. The large recoil-proton angle allows the  $\delta E - E$  counters to be shielded from direct view of the target and the momentum acceptance is equivalent to a  $\theta'_n$  range of  $\sim 4 - 25^\circ$ . The polarimeter does not have full  $\phi'$  coverage and determines the asymmetry from the counting-rate differences in the top ( $\phi' \sim 0$ ) and bottom ( $\phi' \sim \pi$ ) arrays of counters (see Eq.12).

**Counting Rate and Livetime** Both Pol-A and Pol-C have forward veto counters to provide essential particle-identification capability, and here the counting rate is extremely important. Pol-A rates are discussed in Sec. 4.2 and veto-tile rates would not be expected to exceed 0.1 MHz. To estimate the rates expected in E12-11-009, the observed singles rates from a previous Hall-C experiment [11] have been scaled by the ratio of luminosities proposed in E12-11-009 to those used in Ref. [11] (a factor 3.3) and also by the ratio of solid

angles subtended by forward elements of the polarimeters. This yields a rate, for each forward veto counter and first analyzer counter of Pol-C, of approximately 3 MHz. Assuming a dead time for photomultiplier signals of  $\sim 50$  ns, which also includes discriminator dead time and TDC double-pulse resolution effects, the live time in individual counters running at  $\sim 3$  MHz will be  $\sim 85\%$ . For every hit in the Pol-C analyzer there are at least three veto counters which could produce a correlated signal for an incident charged particle. When one of the three veto counters or a selected analyzer counter is dead, an event is effectively lost, so that the overall live time would be  $0.85^4 = 52\%$ . The Pol-A live time would be  $> 99\%$ .

**Shielding Requirements** The elements of the Pol-A analyzer array are aligned with their long axes parallel to the incident particles. This provides good angular resolution and each element presents a smaller area to the target. The timing resolution remains good for the parallel-aligned bars and the array covers the full angle range defined by the SBS dipole aperture. Background rate estimates (Sec. 4.2) indicate that the Pol-A analyzer will function effectively with relatively minimal lead shielding of 50 mm thickness. For Pol-C the proposed polarimeter shielding is 150 mm thick, so that  $p - n$  interactions in the Pb will present a greater potential source of asymmetry dilution.

**Spin Rotation** Polarimetry by  $N - N$  scattering is insensitive to the longitudinal component of spin  $P_z$ , which must be rotated into the transverse plane. Pol-A employs a horizontal magnetic field to rotate  $P_z \rightarrow P_y$  and  $P_x$  and  $P_z$  are determined simultaneously at a single magnetic field setting. An integrated field of  $\sim 2$  Tm in the SBS dipole will produce an angle of rotation close to  $90^\circ$ , where uncertainties in the rotation angle will have the minimum effect on  $P_y$ . Some mixing of  $P_x$  and  $P_z$  will occur in Pol-A, due to fringe fields and different paths through the the dipole. Assuming that the field characteristics are well determined, this can be corrected with good accuracy, as demonstrated in Sec.3.2.5.

Pol-C uses a vertical field direction and  $P_z$  is rotated by varying amounts into the  $x$  direction by varying the magnetic field. This will change the background levels in the polarimeter and hence the potential systematics of the asymmetry, due to changes of the running conditions. Experiment E12-11-009 proposes to use integrated field strengths up to  $\sim 4.5$  Tm where the dipole field will be highly saturated and systematic distortions difficult to quantify.

**Comparison of Precision for Equivalent Running Conditions** Table 1 compares the experimental precision quoted by E12-11-009, using Pol-C, with an estimate of the precision obtainable by the present apparatus, for the values of  $Q^2$  quoted in E12-11-009. Equal measurement times have been assumed and the luminosities are as quoted in the present proposal and E12-11-009. The same values of  $G_E^n$ ,  $G_M^n$  and  $A_Y$  (brown triangles of Fig.9) as quoted in E12-11-009 have been employed. No attempt has been made to differentiate the effective analyzing powers of the two polarimeters, although the Pol-A acceptance is more effective for high-momentum neutrons. Although the values of  $Q^2$  are identical, the employed beam energies and scattering angles are different, due to the different characteristics of the spectrometers.

$Q^2$ (GeV/c) <sup>2</sup>	$\langle p_n^{lab} \rangle$ (GeV/c)	$A_y$ (%)	$\delta R/R$ (Pol-A)	$\delta R/R$ (Pol-C)
3.95	2.901	0.072	0.035	0.101
5.22	3.571	0.058	0.107	0.127
6.88	4.48	0.046	0.106	0.163

Table 1: Comparison of the obtainable experimental precision, expressed in terms of  $\delta R/R$ , where  $R = G_E^n/G_M^n$ , at the values of  $Q^2$  requested in E12-11-009 [59].  $\langle p_n^{lab} \rangle$  is the average momentum of neutrons incident on the polarimeter,  $A_Y$  is the effective analyzing power, Pol-A refers to the present experimental apparatus and Pol-C refers to values given in E12-11-009.

It can be seen that the present apparatus has significantly higher efficiency than experiment E12-11-009, even before the estimated dead-time losses in Pol-C (Sec. 2.6.1) are accounted for. If these are factored in, the Pol-C uncertainties increase by a factor  $\sim \sqrt{2}$ .

Other aspects of the present apparatus, while not superior to E12-11-009, are more than adequate for the present experiment and present no significant compromising of performance.

- BigBite, with a  $\sim 1$  mr angular resolution and a momentum resolution of  $\sim 0.5\%$ , is well suited to the quasi-elastic scattering process, where little is gained by having very high resolution. The GEM high-resolution tracking system will remove limitations on BigBite luminosity, imposed by the previous MWDC trackers.
- The SBS dipole at an integrated field strength of  $\sim 2$  Tm induces a spin precession angle  $\chi > 70^\circ$ , so that after precession  $P_y \gtrsim 0.94P_z$ , where  $P_z$  is the original longitudinal component. The magnetic field also gives very clean separation of neutrons and protons and sweeps all particles of momentum  $< 750$  GeV/c out of the polarimeter acceptance.

Details of the present apparatus can be found in Sec.3.

### 3 Experimental Method

The polarization transfer method requires a large number of counts, because of the relatively low analyzing power of the polarimeter. Going to high momentum transfer, where the effective elastic scattering rate scales approximately as  $E_{\text{beam}}^2/Q^{16}$ , requires high luminosity, large acceptance and a high rate capability in the detection system. A plan view of the detector apparatus is displayed in Fig.10.

We propose to perform the measurement in Hall-A of Jefferson Laboratory, using the CW, polarized electron beam from the CEBAF accelerator. This will have a maximum energy of 11 GeV and maximum current of  $80 \mu\text{A}$ . The present experiment will not require 11 GeV and we have chosen beam energies (Table 2) at integral factors of the standard 2.2 GeV energy gain per pass. This will be the normal operational mode for the accelerator. Beam polarizations in excess

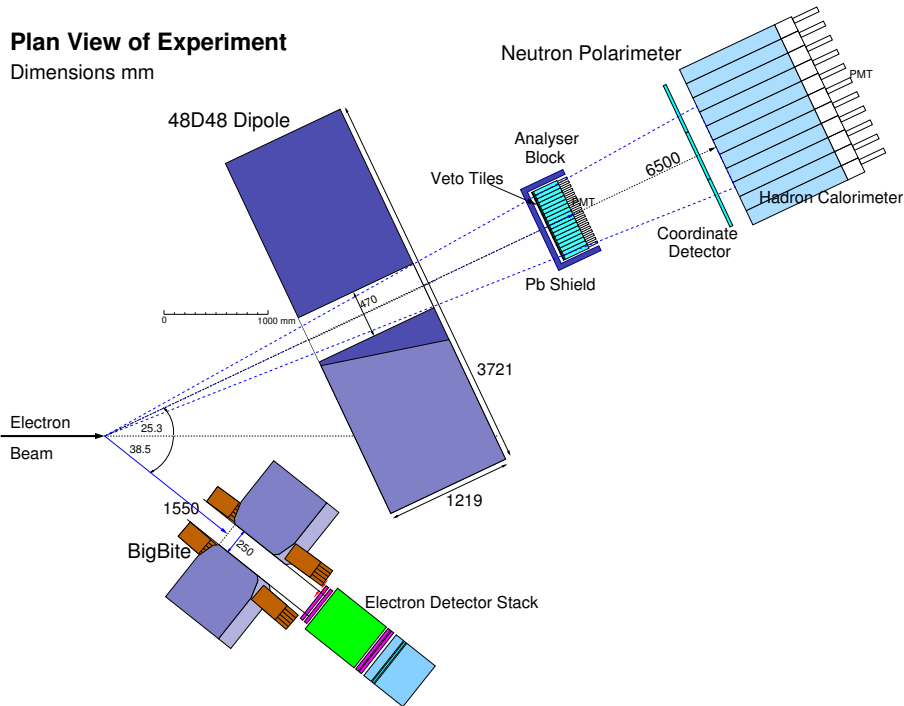


Figure 10: Plan view of experiment  $Q^2 = 4.0 \text{ (GeV/c)}^2$ .

of 80% have been achieved routinely during 6 GeV operation of CEBAF and 80% is assumed for estimates of precision in measuring form factor ratios.

The electrons will be incident on a 10 cm long liquid deuterium ( $\text{LD}_2$ ) target with  $100 \mu\text{m}$  Al entrance and exit windows, giving  $\sim 0.054 \text{ g/cm}^2$  of material, compared to  $\sim 1.69 \text{ g/cm}^2$  for the  $\text{LD}_2$ . A liquid hydrogen ( $\text{LH}_2$ ) target will also be used for calibrations. A  $40 \mu\text{A}$  electron beam incident on a 10 cm  $\text{LD}_2$  target produces an electron-neutron luminosity of  $\sim 1.26 \times 10^{38} \text{ cm}^{-2}\text{s}^{-1}$ .

Scattered electrons are detected in the BigBite spectrometer, which will reconstruct the momentum, direction and reaction vertex, as well as correlating the trigger time to an accelerator beam bunch. The neutron arm will be a polarimeter which consists of a plastic scintillator analyzer block, equipped with charged-particle veto tiles, followed by a further charged-particle veto system and the hadron calorimeter HCAL. The polarimeter will provide position and time-of-flight information for the recoiling nucleon, as well as scattering asymmetries. Neutron spin precession will be performed by the “48D48” dipole which is the basis of the SBS charged-particle spectrometer. The experimental components are described in more detail in the following subsections.

### 3.1 The $e'$ Detector BigBite

BigBite (Fig.11) is a large-acceptance, non-focusing magnetic spectrometer which, when positioned with the entrance aperture of the dipole 1.55 m from the target center, subtends a solid angle of  $\sim 60 \text{ msr}$ . Fig. 11 shows BigBite equipped

with lead glass pre-shower and shower counters to provide a trigger which is insensitive to low energy background. In conjunction with a gas Cherenkov, these counters distinguish electrons cleanly from  $\pi^-$ . Event timing is performed by a plastic scintillator hodoscope consisting of 90  $600 \times 25 \times 26$  mm bars of EJ200 plastic. Tracking is performed by two  $400 \times 1500$  mm Gas Electron Multiplier (GEM) chambers at the front, followed, after a flight path of  $\sim 650$  mm, by a two  $500 \times 2000$  mm GEM chambers. The GEM trackers supercede the MWDC, used in pre-upgrade experiments, and offer increased counting rate capability, so that higher luminosities may be achieved. At CERN they have proved capable [73] of operating at incident fluxes of  $2.5 \text{ MHz/cm}^2$ . They will be assembled from the  $400 \times 500$  mm modules which are being constructed for the SBS program of experiments. The GEM will have a position resolution  $\sigma_r \sim 70 \mu\text{m}$  ( $60 \mu\text{m}$  has been obtained from prototype tests) and the two groups of trackers are separated by around  $0.65 \text{ m}$ . The angular resolution may be estimated from

$$\delta\theta = \sqrt{\left(\frac{\sigma_r}{z_{tr}}\right)^2 + \left(\frac{13.6}{\beta c p_e} \sqrt{\frac{x}{X_0}} \left[1 + 0.038 \ln\left(\frac{x}{X_0}\right)\right]\right)^2} \quad (18)$$

where  $p_e$  is the electron momentum in MeV/c and  $x/X_0$  is the thickness of intervening material in radiation lengths. This translates to an angular resolution of  $\sigma \sim 1 \text{ mr}$  in both dispersive and non-dispersive directions. For the relatively small deflection obtained with an integrated field strength of  $1.2 \text{ Tm}$  and electrons of  $1\text{--}3.5 \text{ GeV/c}$ , the angle of deflection is given by:

$$p_e \approx \frac{e \int B \cdot dl}{\theta} \quad (19)$$

The momentum resolution of  $\delta p/p \sim 0.5\%$  will be entirely adequate for the present experiment (Sec.4.3). The z-vertex resolution at the target is around 4 mm. It is extremely important to have an accurate knowledge of the vertex and four-momentum of the virtual photon, so that the BigBite optics and vertex reconstruction will be calibrated at each kinematic setting, using a sieve slit and multi-carbon-foil target. Momentum will be calibrated using elastic  $ep$  scattering from a  $\text{LH}_2$  target.

Timing from BigBite is provided by a plastic scintillator hodoscope. For high luminosity operation a new, finer granularity, hodoscope is being constructed. This will consist of 90 plastic scintillator elements, each  $25 \times 25 \times 600$  mm, each read out by 2, 9125 photomultipliers (PMT). The intrinsic timing resolution of this device should be around  $0.5 \text{ ns}$  FWHM.

Offline charged particle identification is aided by the threshold gas Cherenkov. Light is collected by a cylindrical mirror and reflected on to a set of around 700 9125 PMT's. Compared to a previous gas Cherenkov, which used 5" PMTs, the new detector will have superior counting rate capability and will be much less susceptible to soft background from the electron beam line.

The Pb-glass pre-shower - shower trigger detector is quite insensitive to charged pions but does not discriminate electrons from  $\pi^0$  decay photons. The new Cherenkov detector will help to discriminate such events. However, if any further reduction of BigBite trigger rates becomes necessary, we envisage to use a "pixel fast readout" GEM chamber where the readout board is arranged in

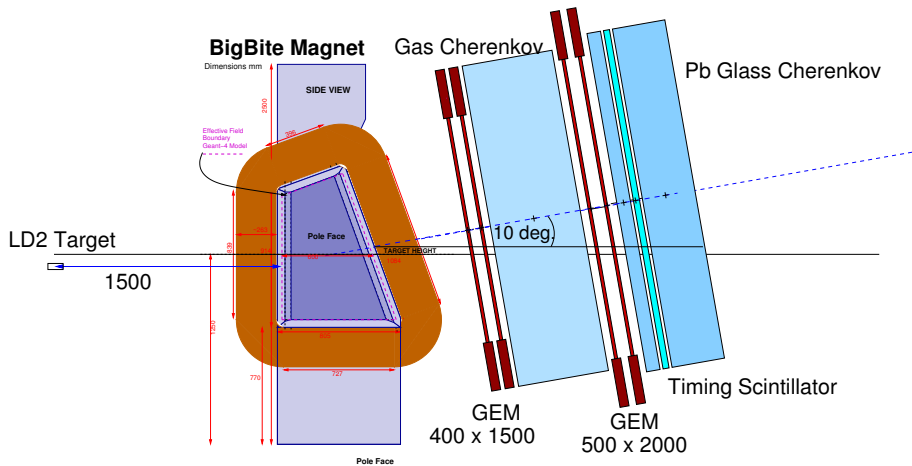


Figure 11: Side view of BigBite as configured for  $e'$  detection

$50 \times 50$  mm pads. It is possible to read a fast signal directly from each pad which has dimensions suitable for hardware coincidences with the Pb-glass counters. BigBite rates are discussed in Sec. 4.2.

### 3.2 The Neutron Polarimeter

The neutron polarimeter (Fig. 10) consists of four main components:

1. An array of plastic scintillator blocks aligned with their long axes parallel to the direction of the recoiling neutrons. This acts as an active polarization analyzer through the azimuthal modulation of the neutron-nucleus scattering cross section.
2. An array of plastic scintillator veto tiles, sited directly in front of the analyzer provide charged particle identification.
3. A charged particle identification system sited directly in front of the hadron calorimeter.
4. A hadron calorimeter HCAL, which is optimized to detect nucleons with momenta of 1.5 - 10 GeV/c with high efficiency. This segmented calorimeter, together with the segmented analyzer array, determines the scattering angle of the neutron used to analyze the spin polarization of the recoiling neutron.

A reduced-scale version of the device proposed here will be built for neutron analyzing power measurements at the Nuklotron accelerator at JINR in Dubna and a proposal [74] to measure the analyzing power up to  $p_n \sim 6$  GeV/c has been accepted. However, operation of the Nuklotron has been delayed and it now seems unlikely that polarized beams will be available before the end of 2013.

### 3.2.1 The Plastic Scintillator Analyzer Array and Veto Detector

The analyzer consists of a  $18 \times 48$  array of  $40 \times 40 \times 250$  mm bars of EJ-200 plastic scintillator [75], aligned with their long axes parallel to the incident neutrons. Each bar will be read out by a 28 mm ETL 9125 PMT of the type used originally in the DIRC detector of BABAR [76]. The original voltage dividers, designed for a few-photon detection situation, are not suitable for the present analyzer array and an alternative design suitable for high-rate scintillation counting will be implemented for the present experiment. PMT's are attached on the downstream side of the detector modules. Neutrons will interact all along the 25 cm length of the analyzer bars giving an uncertainty in flight path and hence time of flight. This is partially compensated by the transit time of scintillation light ( $\eta_{scint} \sim 1.5$ ,  $\beta \sim 2/3$ ) to the PMT photo cathode, and taking both analyzer length and target length into consideration the flight time uncertainty is  $\sim 0.4$  ns for 1.5–3 GeV/c nucleons. The ETL 9125 has a linear focused dynode structure which minimizes time uncertainties in the electron transport. If one estimates the intrinsic timing resolution of the PMT for scintillation counting to be  $\sim 0.75$  ns FWHM (the resolution quoted in [76] is 3.5 ns FWHM for single-photon counting) then the overall timing resolution would be  $\sim 0.9$  ns FWHM.

A finely segmented analyzer is obviously desirable in terms of its position resolution (see Sec.4.1.1) and counting rate. The  $40 \times 40$  mm cross section represents a reasonable compromise in terms of cost and compatibility with the available PMT's. A simulation of the effect of analyzer-bar size on resolution is presented in Sec.4.1.1. Counting rates in the analyzer are discussed in Sec.4.2.

### 3.2.2 Forward Detector for Charged-Particle Identification

In front of the analyzer array comes a set of  $80 \times 80 \times 10$  mm tiles of plastic scintillator, each covering  $2 \times 2$  analyzer bars. These will aid the distinguishing of incident charged and neutron particles, especially in cases where incident particles interact with the Pb shield. Scintillation readout will employ optical fibers.

### 3.2.3 The HCAL Hadron Calorimeter

Downstream of the tracker comes a  $11 \times 24$  array of calorimeter modules [49] (Fig.12). These modules were originally designed for hadron detection in the 10 - 100 GeV range, but Monte Carlo simulations (Sec.4.1) have already predicted that they will perform well in the 1.5 - 10 GeV domain. They are formed from a sandwich of Fe and plastic scintillator plates of total thickness 1 m and a Fe-to-plastic thickness ( $\text{g}/\text{cm}^2$ ) ratio of 11:1, optimized for JLab energies.

Scintillation light is collected on a wavelength-shifting guide and then piped to a PMT. These modules form the basis of the planned SBS calorimeter HCAL. Their efficiency and resolution for few-GeV incident nucleons is discussed in Sec.4.1.2. The time resolution of the COMPASS modules was around 1.5 ns, but this will be improved substantially by using a faster fluorescent dye in the wavelength-shifting guide. In conjunction with the (BaBar) 9125 PMTs, this will provide a shorter pulse rise time and shorter pulse length. Processing of

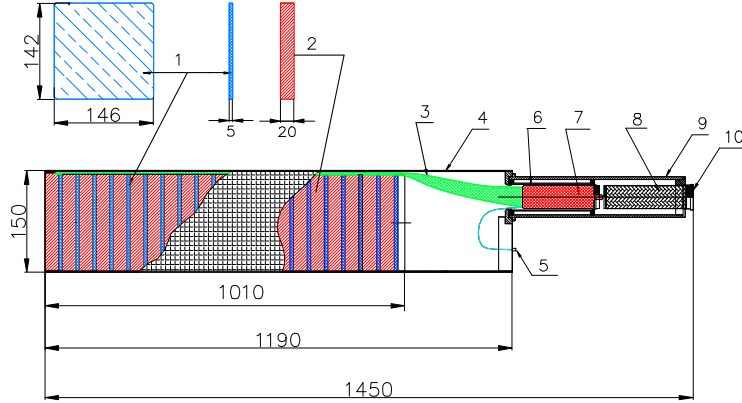


Figure 12: Diagram of a single calorimeter module from Ref.[49]. Components are labeled 1: scintillator sheets; 2: Fe sheets; 3: wavelength-shifting, scintillation readout sheet; 4: metal container; 5: diagnostic optical input; 6: magnetic shield; 7: PMT; 8: PMT HV divider;

this pulse is performed by flash ADC hardware which has an order of magnitude higher sampling rate than the original COMPASS hardware. Thus precise time reconstruction of the fast pulse form will be possible.

### 3.2.4 Rear Detector for Charged-Particle Identification

A “coordinate detector” (CD), based on  $3 \times 30 \times 1000$  mm plastic scintillator strips, is under design [77] for use on the electron arm of the GEp(5) experiment [8]. There the CD would be used in conjunction with an electromagnetic calorimeter to identify electrons and provide good hit-coordinate resolution. The CD modules would also be suitable for this experiment, where the electron-arm spectrometer is BigBite, and would be placed before HCAL to differentiate scattered charged from neutral particles in the polarimeter.

The CD readout will be by 2 mm WLS optical fibres, connected to multi-anode PMTs, which have been procured from FNAL. The projected time resolution is  $\sim 0.5$  ns, which will allow tight coincidence conditions to be made between the CD, the Analyzer array and HCAL. The efficiency of one CD layer is around 92% for minimum-ionising particles and the rate capability will be high, to function effectively in the much higher luminosity GEp(5) experiment.

### 3.2.5 The 48D48 Dipole

The SBS uses a single dipole for magnetic analysis which has an open geometry, meaning that the detector is in direct view of the target. This approach provides

a large solid angle and hence improved statistics and of course is suitable for a neutron-arm detector.

For quasi-elastic neutron detection the dipole (known as 48D48) has no direct use as a spectrometer, but it serves several purposes:

1. To precess the spin of the recoiling neutron from the longitudinal to the vertical direction. The nucleon polarimeter measures transverse components of spin only.
2. To deflect protons produced in quasi-elastic  ${}^2\text{H}(e, e'p)$ . These are then separated from quasi-elastic neutrons through angular correlations with the  $\vec{q}$  vector determined from the electron arm. The vertical deflection, calculated from the reconstructed hit position at the Analyzer, is displayed as a function of nucleon momentum, in Fig.13. The incident nucleon angles cover the full vertical acceptance of the 48D48 dipole. Calculations have been made with and without the 50 mm Pb shield. Scattering in the shielding obviously smears the reconstructed-position difference, but with 50 mm Pb, neutron-proton separation remains good at  $p_N = 4$  GeV/c. Without the Pb, proton contamination amounts to  $<1\%$  of the neutron signal, while with the Pb it is  $\sim 2\%$ . Particle identification in the Analyzer is augmented by a forward set of 10 mm thick, plastic veto tiles.
3. To sweep low-momentum, charged background out of the acceptance of the polarimeter. The cut-off momentum for charged particles can be gauged from Fig.13. For an integrated field strength of 2 Tm, all charged particles of momenta below  $\approx 0.78$  GeV/c are swept beyond the Analyzer.

The use of a single dipole spectrometer to precess the spin of the recoil nucleon has the advantage of simplifying the spin transport calculation, compared to a multiple-magnet spectrometer such as the HRS. Neutron spin precession through the dipole field has been calculated using the polarimeter Monte Carlo model. Non-perpendicular incidence with respect to the field direction, e.g. due to fringe fields and an extended angular range, produces small rotations in the  $z-x$  plane which can affect  $P_x/P_z$  and hence  $G_E/G_M$ .

The 48D48 dipole, modified for use in Hall A, is not yet installed and thus an accurate field map is not available. However, we have calculated the size of possible  $z-x$  mixing effects using field maps obtained using the 3D code TOSCA [78]. The employed field map calculation (Fig. 14) has not included any field clamps to the bare dipole and thus represents a worst-case scenario in terms of the stray field, which extends beyond the confines of the dipole aperture. At a coil excitation of  $\sim 2000$  A, an integrated field strength of  $\sim 2$  Tm is calculated, which produces a spin rotation  $z \rightarrow y$  of  $\sim \pi/2$ . Neutrons with an initial polarization  $\mathbf{P} = (0, 0, 1)$  and a momentum of 3 GeV/c were tracked through the dipole field and their polarization recorded when they impinge on the analyzer. The value of  $P_x$  (Fig. 14), calculated after passing through the field, is at the few % level and varies smoothly as a function of the hit position. If the maximum degree of spin transfer  $z \rightarrow x$  is  $\sim 0.05$  and the expected ratio  $P_x/P_z$  in a  $G_E^n/G_M^n$  measurement is  $\sim 0.2$ , then the maximum error induced in a measurement of  $P_x/P_z$  will be  $\sim 25\%$ . Given that the analyzer will have a position resolution of  $\sim 1$  cm, and the maximum gradient  $\delta P_x/\delta x$  is  $\sim 0.005/cm$ ,

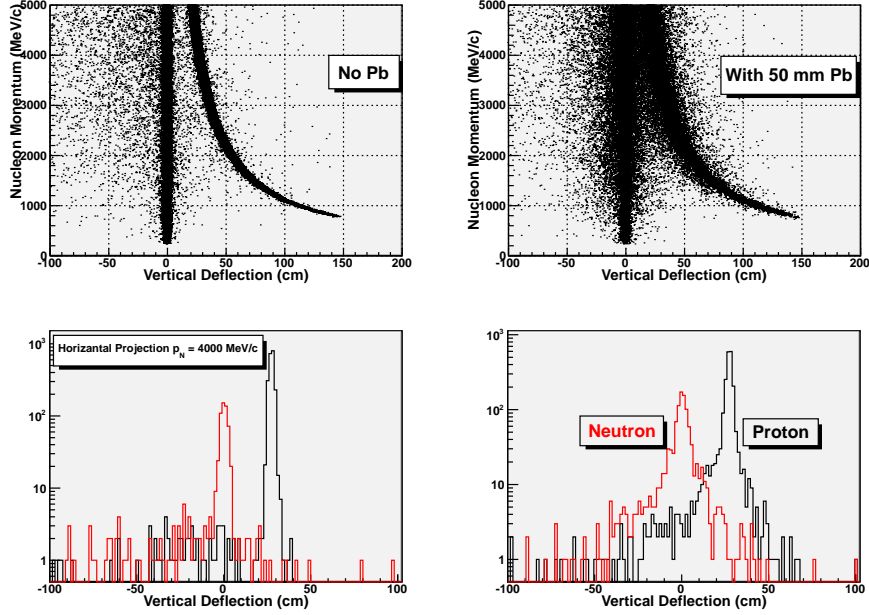


Figure 13: Separation of proton and neutron events

Setting	$Q^2$ (GeV/c) <sup>2</sup>	$E_e$ (GeV)	$p_{e'}$ (GeV)	$\theta_e$ (deg.)	$\theta_n$ (deg.)
1	1.5	2.2	1.40	40.8	38.8
2	2.0	2.2	1.14	52.8	31.1
3	3.0	4.4	2.81	28.5	34.7
4	4.0	4.4	2.24	37.3	27.5
5	6.0	6.6	3.40	30.0	25.0

Table 2: Kinematic Settings. Elastic  $n(e,e'n)$  values

the maximum error after correction will be  $\sim 2.5\%$ . The size of the effect, integrated over the angular acceptance of the SBS dipole, will be considerably smaller.

### 3.3 Kinematics

Kinematic settings have been calculated for  $Q^2 = 1.5, 2.0, 3.0, 4.0,$  and  $6$  (GeV/c)<sup>2</sup> and are summarized in Table 2. The nominal “central” values of the momenta and angles relate to free  $n(e,e'n)$ . Beam energy settings employ the standard energy gain per turn of 2.2 GeV.

The ranges of kinematic variables for the nominal settings of the large acceptance detector system were calculated for quasi-free  ${}^2\text{H}(e,e'n)$ , where the internal momentum distribution of the neutron was sampled from  $p_N^2 \cdot \exp(-p_N^2/2\sigma_N^2)$ ,  $\sigma_N = 0.03$  GeV/c, i.e. the Fermi distribution was approximated by a Gaussian of width 0.03 GeV/c. Events were generated along the 10 cm length of the target and scattered electrons were detected within the effective  $250 \times 750$  mm

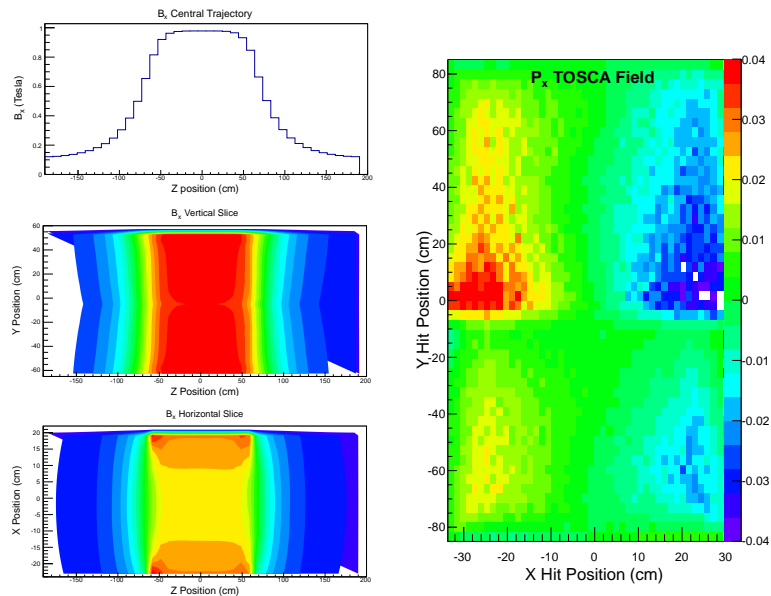


Figure 14: Left: Position dependence of  $B_x$  generated by TOSCA. Right: induced spin component  $P_x$  through TOSCA field.

aperture of BigBite situated  $\sim 2$  m from the target center. It was also checked if the recoiling neutron is within the acceptance of the 48D48 aperture. BigBite subtends a solid angle of  $\sim 58$  msr and between 70 and 95% of correlated neutrons pass through the aperture of the 48D48. Fig. 15 displays the calculated coverage in  $Q^2$  while the BigBite angular acceptance and corresponding  ${}^2\text{H}(e, e'n)$  neutron acceptance are shown in Fig.16 for the kinematic settings of Table 2.

## 4 Determination of the Ratio $G_E^n/G_M^n$

The ratio  $G_E^n/G_M^n$  will be determined from the scattering asymmetries measured in the recoil neutron polarimeter. The following subsections describe the Monte Carlo simulations of the response of the detector systems, calculations of background rates in the detector systems, the techniques employed to isolate the quasi-elastic signal and finally a discussion of the systematic uncertainties.

### 4.1 Modeling the polarimeter

Monte Carlo simulations [79] of the experiment have been performed within the framework of the the Geant-4 software toolkit. Standard Geant-4 does not consider polarized nucleon scattering and extensions to the hadron-interaction classes have been written. These use fits to published analyzing power data to modify the azimuthal distributions of nucleons produced in elastic or quasi-elastic processes. The original code was developed [80] originally as part of the

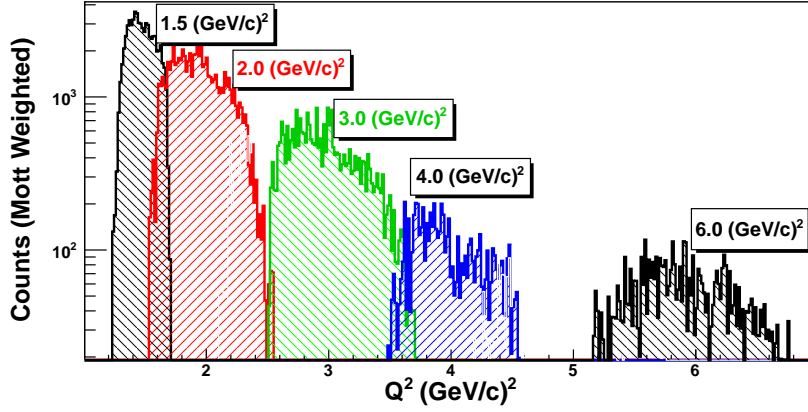


Figure 15: Range of  $Q^2$  for the nominal settings labeled on the plot. The distributions are weighted by the Mott cross section (Eq.5).

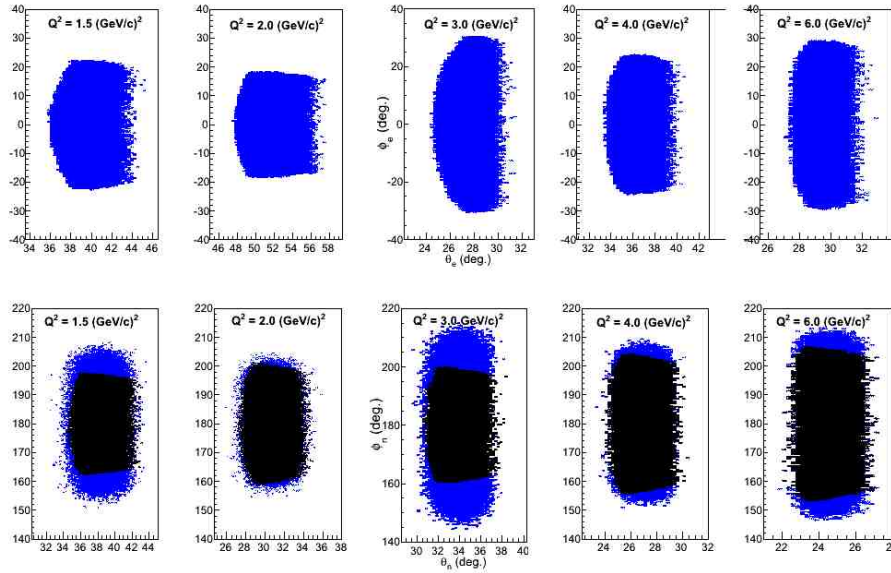


Figure 16: Top row: angular coverage of BigBite, x-axis  $\theta_{e'}$ , y-axis  $\phi_{e'}$ . Bottom row (blue)  $d(e, e'n)$  neutron angles (x-axis  $\theta_n$ , y-axis  $\phi_n$ ) corresponding to  $e'$  hits in BigBite (see corresponding upper plot). Bottom row (black)  $d(e, e'n)$  neutron angles which pass through the aperture of the SBS dipole.

analysis of the experiment to measure  $G_E^n/G_M^n$  by recoil polarimetry at Mainz [68].

A brief description of the polarized-scattering model follows:

- Polarization is considered only when the original particle is a nucleon and the material through which tracking is performed contains H or C. Otherwise the standard unpolarized Geant-4 event sampling of azimuthal angle is performed.
- The “leading nucleon” produced by an elastic or quasi-elastic hadronic reaction process, i.e. with the highest kinetic energy, is identified. If there is no “leading nucleon” the scattering is considered unpolarized.
- The analyzing power for elastic processes are determined on the basis of incident momentum and scattering angle, using fits to previous experimental data. Several different parametrizations are available for use when sampling azimuthal distributions.
- The rotation in scattering azimuthal angle is sampled with a weighting determined by the transverse component of the incident polarization and the analyzing power.
- This process is repeated if there are multiple elastic scattering events in the analyzer material. In multiple scattering the original reaction plane is lost, effectively depolarizing the nucleon.

The geometry and materials of the analyzer block and calorimeter are modeled realistically using standard Geant-4 tools. At this stage the analyzer, calorimeter and the 48D48 dipole have been modeled fairly realistically. Electromagnetic interactions are modeled within Geant-4 using the so called extended implementation, while the hadronic interactions include:

- Coherent nucleon-nucleon elastic scattering: this method is called for incident energies up to 1.2 GeV. The cross sections are derived from the SAID database.
- Nucleon-nucleus elastic scattering at medium to high energy: the Glauber model is used to calculate differential cross sections for elastic and quasi-elastic nucleon-nucleus scattering. Inelastic screening corrections are implemented at high energy.
- Hadron-nucleus inelastic scattering: this is performed using the so-called Bertini Intranuclear Cascade model. The cascade begins when the incident particle strikes a nucleon in the target nucleus, producing secondaries. These may escape, produce more secondaries or become absorbed. The process continues until all particles with sufficient energy escape the nucleus. This model been tested against data at energies in the range  $\sim 0.1 - 5$  GeV.

Monte Carlo data generated by the Geant-4 model were analyzed, as if they were experimental data. The Monte Carlo data stream contains the sensed energies, times etc. from detector elements, along with the actual 4-momenta

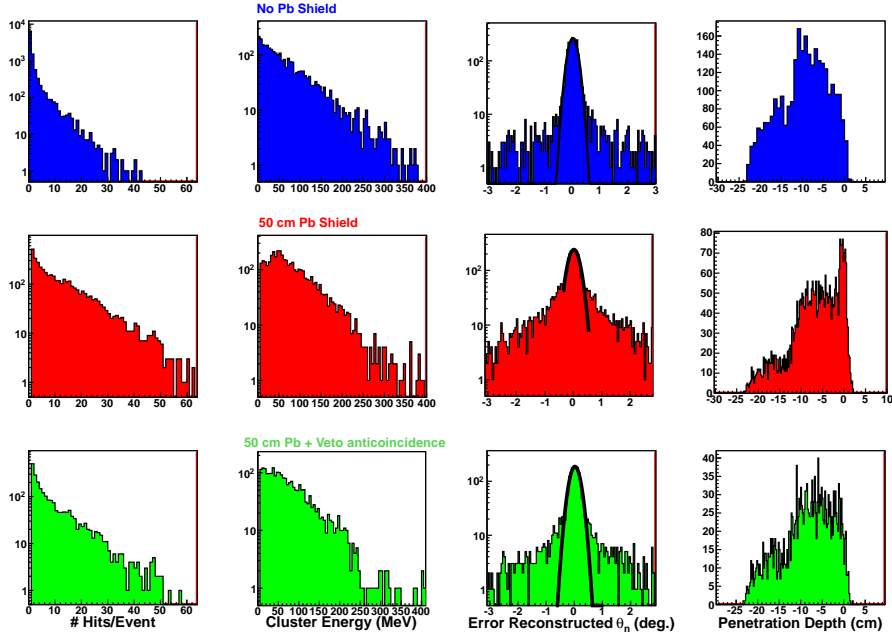


Figure 17: The reconstructed response to 4 GeV/c neutrons of the analyzer array. Left to right: number of analyzer hits per event, the energy in a reconstructed hit cluster, the error in the reconstructed polar angle and the penetration depth before the 1st hit is registered (the front is at position 0 cm). Blue is no Pb shield, red is with a 50 mm Pb shield, green is with the Pb shield and an anti-coincidence cut on the forward veto scintillator.

which produce that response. Thus the error distributions in the reconstructed kinematic quantities can be used to assess energy, time and position resolution. Calculations have been made with and without a Pb wall to shield the analyzer from the target.

BigBite is partially implemented, with the pre-shower, shower and trigger counters in place. A representation of the GEM Chambers is in place, but they are not yet considered in detail. They are modeled in a basic manner as a slab of material with approximately the correct thickness (in terms of  $g/cm^2$ ) which yields hit positions. These are smeared to a degree consistent with the expected resolution. The properties of BigBite have been proven in a list of recent Hall-A experiments and very detailed Monte Carlo software has been written to simulate 6-GeV configurations which are very similar to the present experiment. The following concentrates on the new components of the apparatus on the neutron arm.

#### 4.1.1 The Simulated Response of the Analyzer Block

Simulated neutrons of momentum 4 GeV/c were incident at specific points of the analyzer. Their interactions within the analyzer block produce multiple detector hits per event and “clusters” of hits are reconstructed to produce a cluster energy, hit time and a ( $\sqrt{E}$  weighted) mean position. A cluster is constructed after

$E_{th}$	5	20	40	60	80	100
$\varepsilon$	26.4	21.2	16.0	12.1	9.0	6.9
$\varepsilon_{Pb}$	22.6	19.1	15.0	11.1	8.2	6.0

Table 3: Effective neutron efficiency (%) of the  $40 \times 40 \times 250$  mm analyzer array for  $p_n = 4$  (GeV/c) and ascending values of the threshold energy  $E_{th}$  (MeV).  $\varepsilon_{Pb}$  is the value with a 50 mm lead shield inserted before the analyzer. Polarimeter calculations have been made with an analyzer threshold of 20 MeV.

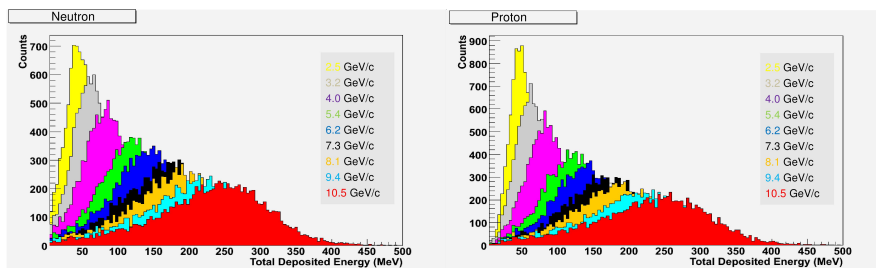


Figure 18: HCAL pulse height response to neutron (left) and protons (right).

finding a detector element with a maximum in energy deposit and then scanning for a signal in the  $5 \times 5$  array with this element at the center. Timing resolution is discussed in Sec.3.2.1.

Calculations have been made for detector elements of  $30 \times 30$ ,  $40 \times 40$  and  $50 \times 50$  mm cross section and lengths of 250 mm and 500 mm. Calculations have also been made with a 50 mm Pb wall placed in front of the analyzer array and with a set of 1 cm thick plastic scintillator “veto tiles” placed directly in front of the analyzer. Fig.17 (top row/blue) displays some parameters for  $40 \times 40$  cm elements with no Pb or scintillator before the array. Gaussian fits to the error ( $\sigma$ ) in the reconstructed angle  $\delta\theta_n$  produce  $\delta\theta_n = 0.12^\circ$ ,  $0.17^\circ$ ,  $0.21^\circ$  for bar cross sections  $30 \times 30$ ,  $40 \times 40$  and  $50 \times 50$  mm respectively. Introducing the Pb wall Fig.17 (middle row/red) results in scattering and charged conversion of significant numbers of incident neutrons. There is now a front peak in the penetration depth distribution and greater hit multiplicity. In this case  $\delta\theta_n = 0.22^\circ$  and the distribution has more pronounced non-Gaussian “wings”. The situation is improved if a prompt anti-coincidence condition is placed on the prompt timing peak from the forward plastic scintillator, giving  $\delta\theta_n = 0.18^\circ$ .

The effective detection efficiency, the fraction of incident neutrons which register a hit in the analyzer, is given in Table3. With the veto-tile anti coincidence requirement the effective efficiency is reduced slightly when the Pb wall is in place. Angular resolution calculations were made with a cluster threshold of 20 MeV which corresponds to a detection efficiency of  $\sim 20\%$ . Counting rates in the analyzer are discussed in Sec.4.2.

#### 4.1.2 The Simulated Response of the Hadron Calorimeter HCAL

The response of HCAL was also calculated using the simulation, outlined above, and calculations [81] of the response made for the SBS  $G_M^n$  proposal [7] are

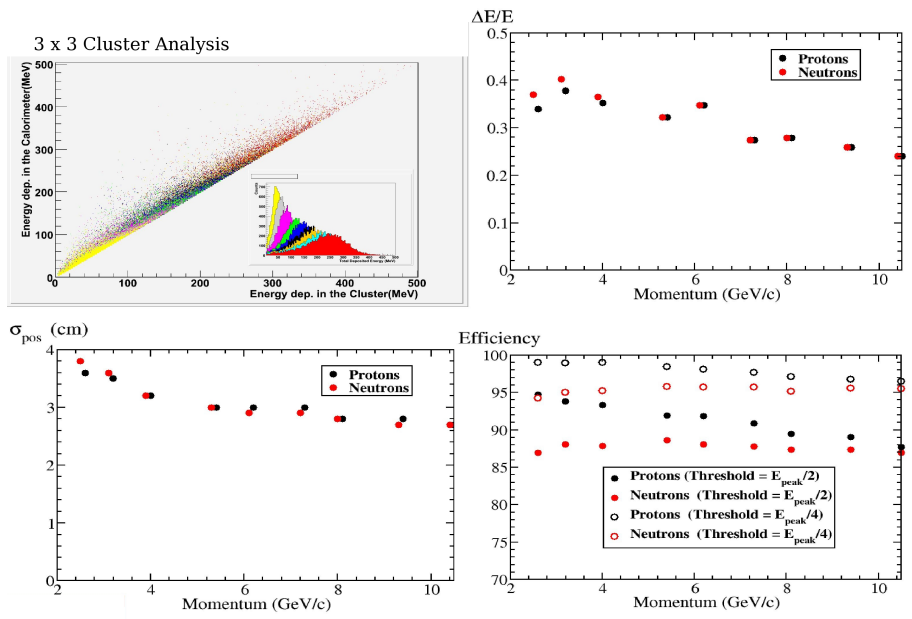


Figure 19: Calculations of HCAL response. Top left: energy leakage from a  $3 \times 3$  hit cluster; top right: fitted energy resolution of the peak region of the pulse height response (Fig.18); bottom left: position resolution from cluster mean position; bottom right: detection efficiency for 2 threshold settings.

displayed in Fig.18 and 19. These calculations were made without any material (except air) in the path of the incident neutrons. The procedure to reconstruct the HCAL response is very similar to that described in Sec.4.1.1. It is clear that the response to neutrons and protons is very similar, with the energy scale in Fig.18 showing the energy loss in the plastic scintillator sheets only. This analysis was made on the assumption that a cluster of hits does not extend beyond a  $3 \times 3$  group, which results in a small leakage of energy outside of this group. The peaked response means that thresholds can be set high to suppress low energy background from the experimental trigger, without large reductions in detection efficiency. A position resolution of around 30 mm results in a resolution for the reconstructed scattering angle of around 12 mr, which is sufficient for selection of “good” scattering angles where the analyzing power is high (Sec.4.1.3).

### 4.1.3 The Simulated Response of the Polarimeter

Analysis of the polarimeter response involves reconstruction of the hits in the Analyzer and HCAL, followed by reconstruction of the polar and azimuthal components of the scattering angle. The scattering asymmetry is then obtained from sine ( $P_x$ ) or cosine ( $P_y$ ) fits to the azimuthal distribution. Any unpolarized variation in azimuthal acceptance is subtracted before the fit is made.

The effects of finite size and imperfect reconstruction of the scattering process have been investigated using the Monte Carlo model. Multiple scattering in the

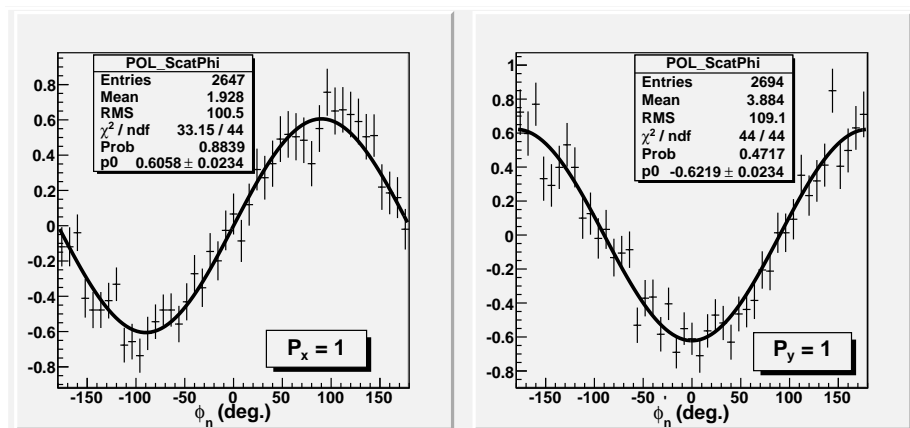


Figure 20: Fits to the simulated azimuthal scattering distributions in the polarimeter for incident polarization  $P_{x,y} = 1$  and  $A_y = 1$ .

$A_z$ (mm)	$A_{x,y}$ (mm)	Pb (mm)	HCAL Thr (% Peak)	$\varepsilon$ (%)	$D_x$ $\theta'_n = 1 - 10^\circ$	$D_y$ $\theta'_n = 1 - 10^\circ$
250	30	0	50	7.2	$0.68 \pm 0.07$	$0.62 \pm 0.06$
250	40	0	50	7.6	$0.70 \pm 0.07$	$0.78 \pm 0.07$
250	50	0	50	7.8	$0.72 \pm 0.07$	$0.69 \pm 0.07$
250	30	50	50	6.5	$0.50 \pm 0.07$	$0.62 \pm 0.07$
250	40	50	50	6.9	$0.60 \pm 0.02$	$0.62 \pm 0.02$
250	50	50	50	7.1	$0.61 \pm 0.07$	$0.66 \pm 0.07$
500	40	0	50	14.1	$0.62 \pm 0.05$	$0.70 \pm 0.05$
500	40	50	50	11.2	$0.61 \pm 0.02$	$0.62 \pm 0.02$

Table 4: Systematic variations of dilution effects in the polarimeter.  $A_z$ ,  $A_{x,y}$  are respectively the length and transverse size of the Analyzer bars, Pb is the thickness of the lead shield, HCAL Thr is the threshold setting in HCAL,  $\varepsilon$  is the calculated polarimeter detection efficiency after selection of angles and  $D_{x,y}$  are the dilution factors for incident  $P_{x,y} = 1$ .

analyzer effectively depolarizes the neutrons as the original reaction plane is lost, but the analyzer also requires to be sufficiently thick that a reasonable efficiency is maintained. Assuming that the optimum analyzing power is obtained if the transverse momentum  $P_t = P_N^{inc} \sin \theta_N \sim 0.45$  GeV/c, the optimum scattering angle  $\theta_N$  will drop from  $\sim 13$  to  $\sim 6$  deg. as the incident momentum rises from 2 to 4 GeV/c. The present geometry of the analyzer and HCAL produces a scattering angle resolution of  $\sim 0.7^\circ$ , which is adequate, and obviously the separation distance can be tuned to suit the scattering kinematics.

Investigations have focused initially on dilution effects in the neutron polarimeter. For this the incident neutrons have been assigned  $P_{x,y} = 1$  and the analyzing power set to 1. Calculations have been made at an incident momentum of 4 GeV/c, with the analyzer threshold set to 20 MeV and the HCAL threshold set at 50% of the peak channel in the pulse-height distribution.

Table 4 lists the Monte Carlo calculated dilution parameters, which are just

the amplitudes of the sine or cosine fits, for different analyzer geometries. The depolarizing effects of scattering in the Pb shield appear to reduce  $D_{x,y}$  slightly. Stretching the Analyzer to 500 mm length increases the detection efficiency without any apparent large reduction in  $D_{x,y}$ .

Higher precision calculations are also proceeding with angle and momentum dependent parametrizations of the analyzing power, which should be more sensitive to depolarizing effects. Provisionally an analyzer thickness of 250 mm has been chosen (Sec.3.2.1).

#### 4.1.4 Determination of $G_E^n/G_M^n$ from Simulated Azimuthal Asymmetries

A simulation has also been made using values of  $P_x$  and  $P_z$  derived from the fit to  $G_E^n(Q^2)$  and  $G_M^n(Q^2)$  in Ref.[83]

$$G_E^n = \sum_{i=1,2} \{a_i/(1 + Q^2/b_i)\} \quad (20)$$

where  $a_1 = -a_2 = 0.095 \pm 0.018$ ;  $b_1 = 2.77 \pm 0.83$ ;  $b_2 = 0.339 \pm 0.046$ . This is the same parametrization as employed in proposal E12-11-009 [59]. The  $n + CH$  analyzing power  $A_y^n(p_n, \theta'_n)$  depends on incident momentum and scattering angle, with the  $n - H$  analyzing power taken from Ref. [52] and the  $n + C$  analyzing power calculated as described in Sec. 2.4.2.

Calculations have been made for 4 combinations of the effective neutron polarizations in the  $x$  and  $y$  directions:  $P_x^* = A_y^{eff} P_e P_x$  and  $P_y^* = A_y^{eff} P_e P_z \sin \chi$ , where  $A_y^{eff}$  is the effective analyzing power,  $P_{x,z}$  are the  $x$  and  $z$  components of the recoil neutron polarization, calculated from [83],  $P_e$  is the electron beam polarization (0.80) and  $\chi$  is the angle of precession from  $z \rightarrow y$  (Table6). Describing the azimuthal distribution as

$$F(\phi'_n) = C\{1 \pm |P_x^*| \sin \phi'_n \pm |P_y^*| \cos \phi'_n\}$$

then the four possible  $\pm$  combinations are labeled  $F_{++}$ ,  $F_{--}$ ,  $F_{+-}$ ,  $F_{-+}$

They mimic the four combinations of beam helicity flip ( $P_{x,y}^* \rightarrow -P_{x,y}^*$ ) and the change of polarity of the 48D48 dipole ( $P_y^* \rightarrow -P_y^*$ ) and may be used to separate the (relatively small)  $x$  component from the  $y$ . The unpolarized background and  $x, y$  components are given by:

$$\begin{aligned} C &= (F_{++} + F_{--} + F_{+-} + F_{-+})/4. & (21) \\ F_{x1} &= (F_{++} - F_{-+})/2C, & F_{x2} &= (F_{+-} - F_{--})/2C \\ F_{y1} &= (F_{++} - F_{+-})/2C, & F_{y2} &= (F_{-+} - F_{--})/2C \end{aligned}$$

$F_{x,y}$  are then fitted with sine and cosine functions to obtain the values of  $P_{x,y}^*$  and their uncertainties  $\delta P_{x,y}^*$ . From this is derived the estimated relative precision  $\delta R/R$  of the ratio  $R = G_E/G_M$ .

$$\frac{\delta R}{R} = \sqrt{\left(\frac{\delta P_x^*}{P_x^*}\right)^2 + \left(\frac{\delta P_y^*}{P_y^*}\right)^2} \quad (22)$$

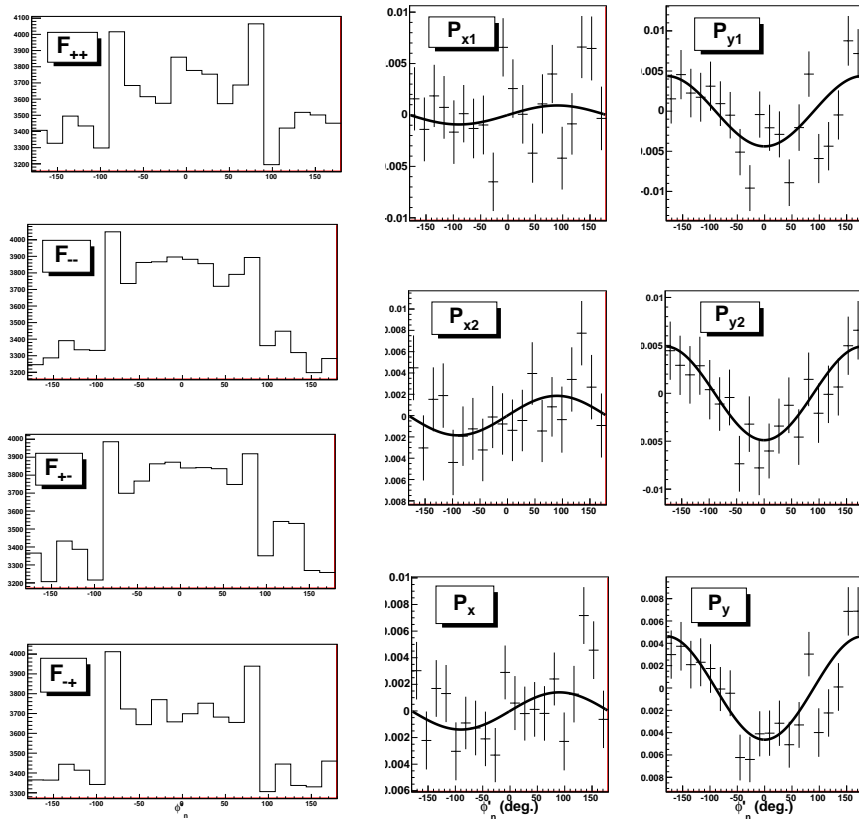


Figure 21: Simulated azimuthal asymmetries. Left: “raw” azimuthal distributions (note the zero is suppressed). Right: fits to separated distributions  $F_x$ ,  $F_y$  (Eq.21). The bottom row right shows the averages of  $F_{x1,2}$  and  $F_{y1,2}$ .

$P_{x1}^*$ $\times 10^{-3}$	$P_{x2}^*$ $\times 10^{-3}$	$P_{y1}^*$ $\times 10^{-3}$	$P_{y2}^*$ $\times 10^{-3}$	$P_x^*$ $\times 10^{-3}$	$P_y^*$ $\times 10^{-3}$	$R_1$	$R_2$	$R$
0.92	1.85	-4.39	-4.89	1.39	4.63	0.21	0.38	0.30
$\pm 0.93$	$\pm 0.93$	$\pm 0.94$	$\pm 0.93$	$\pm 0.66$	$\pm 0.66$	$\pm 0.21$	$\pm 0.20$	$\pm 0.15$

Table 5:  $P_x^*/P_y^*$  Ratio values at an incident momentum of 3.0 GeV/c (bottom row). The input value of R was 0.22.

Fig.21 shows simulated azimuthal scattering distributions made with  $P_x^* = \pm 0.1$ ,  $P_z^* = \pm 0.45$  and  $A_y^{eff}(p_n, \theta'_n)$  calculated as described above. The incident momentum  $p_n$  was 3 GeV/c, slightly above that of the  $Q^2 = 4$  (GeV/c)<sup>2</sup> kinematic setting and the total number of incident neutrons simulated was  $4 \times 10^6$ . The ratio of  $P_x^*/P_y^*$  was derived from the sine and cosine fits to the scattering distributions and is displayed in Table 5. The derived value is consistent with that input to the calculation and the relative uncertainty  $\delta R/R = 0.5$  is consistent with the simple prediction ( $\delta R/R = 0.49$ ) of Eq.14 for  $4 \times 10^6$  incident neutrons. The analysis selected reconstructed, polar-scattering angles in the range  $1 - 10^\circ$ . New Monte Carlo simulations are under way to improve the statistical precision, to allow more quantitative comparisons with the simple estimate (Eq.14) of statistical uncertainty. Pending the results of these calculations, our preliminary conclusion is that Eq.13,14 provide a reasonable approximation when assessing necessary counting time.

## 4.2 Background Rates and the Trigger Rate

Singles rates in detectors have been evaluated using the code DINREG [82], which is well proven in estimating background rates in Hall-A. Fig. 22 displays calculated rates for BigBite, made for the present experiment at  $Q^2 = 1.5 - 4.0$  (GeV/c)<sup>2</sup>. The shower-counter trigger threshold will be set at around 0.65 of  $E_{e'}$  for elastic scattering, which accounts for the range of  $Q^2$  covered by BigBite and also for the momentum resolution. At the settings pertinent to  $Q^2 = 4$  (GeV/c)<sup>2</sup>:  $E_{beam} = 4.4$  GeV,  $\theta_{e'} = 37.3^\circ$ ,  $\Omega_{e'} = 58$  msr,  $\mathcal{L}_n = 1.3 \times 10^{38} \text{cm}^{-2}\text{s}^{-1}$ , the BigBite trigger rate is estimated at  $\sim 50$  kHz, of which 5 kHz is from charged particles and 45 kHz from uncharged ( $\pi^0$ ). Thus a coincidence with the neutron arm will be desirable for triggering purposes.

Fig. 23 shows equivalent calculations for the neutron arm detectors, made with an integrated field strength of 1.7 Tm which will sweep charged particles of momenta  $\lesssim 650$  MeV/c out of the analyzer acceptance. N.B. these calculations have been made at  $\mathcal{L}_n = 5 \times 10^{38} \text{cm}^{-2}\text{s}^{-1}$ , twice that proposed here. The kinematic setting is for  $Q^2 = 4$  (GeV/c)<sup>2</sup>, where the recoil neutron momentum is  $\sim 3$  GeV/c.

On the bottom are the rates in the analyzer array. The trigger level (in MeV electron equivalent) and the rate refer to individual scintillator bars. Note that calculations in previous technical sections are also in electron equivalent units, which account for a non-linear pulse height response from non-relativistic particles. For the present case the rate in individual analyzer bars, for a threshold of 5 MeV, will be  $\sim 0.1$  MHz, which is well within the capabilities of a fast plastic scintillator.

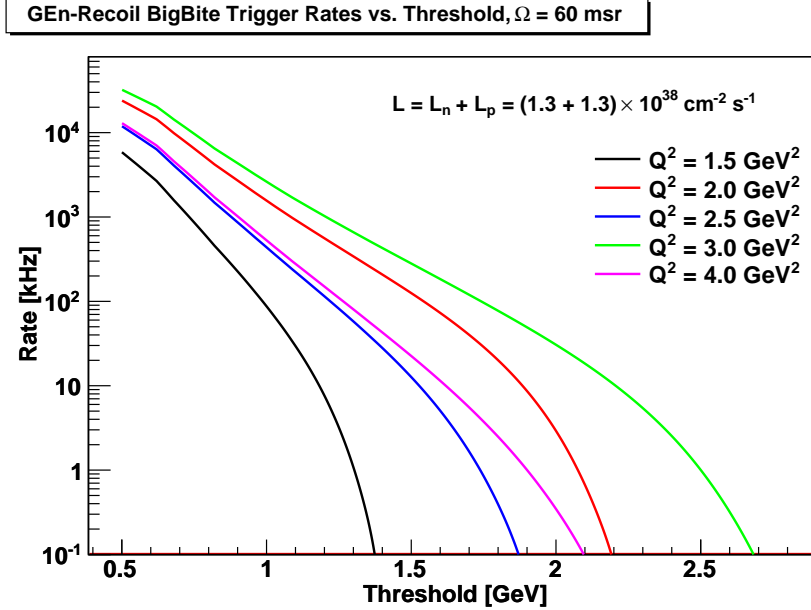


Figure 22: BigBite rate calculations for the present kinematic settings at  $Q^2 = 1.5 - 4.0 \text{ (GeV/c)}^2$ .

On the top of Fig.23 is the combined rate in a  $4 \times 4$  cluster of HCAL modules. For incident neutrons of  $\sim 3 \text{ GeV/c}$  the trigger threshold will be  $\sim 30 \text{ MeVee}$  (1/2 of the peak value in the pulse height distribution) and the cluster rate is 100 kHz, which translates to a total rate of 1.5 MHz in the calorimeter.

With 50 kHz in BigBite, 1.5 MHz from HCAL and a coincidence window of 50 ns, the accidental rate will be  $\sim 4 \text{ kHz}$ . This may yet prove to be uncomfortably high for the DAQ system. With improved fast photon-electron selection in the BigBite trigger, the rate would be reduced significantly. We will investigate the effect of the new BigBite Cherenkov on trigger decisions. Alternatively the effect of a pixelated veto detector, placed directly in front of the BigBite shower counter, is being considered. A fast detector with pixel-geometry readout (e.g. scintillator-tile or GEM) would have good electron efficiency, but low photon efficiency, so that photon background would be suppressed. Fast signals, derived from  $\sim 5 \times 5 \text{ cm}$  pads, would be correlated to the Pb-glass blocks behind, in fast FPGA hardware feeding into the trigger system.

Based on rates observed in drift chambers during the GEN(1) experiment, a  $5 \times 5 \text{ cm}$  pad would, in the present experiment, run at around 1.25 MHz. At 50 ns coincidence resolving time, correlations between 400 pads and 189 Pb-glass shower counters would be made in a FPGA based trigger filter, which is part of the SBS apparatus. This would reduce the rate to  $\sim 1 \text{ kHz}$ , which would be well within the capabilities of the present DAQ system.

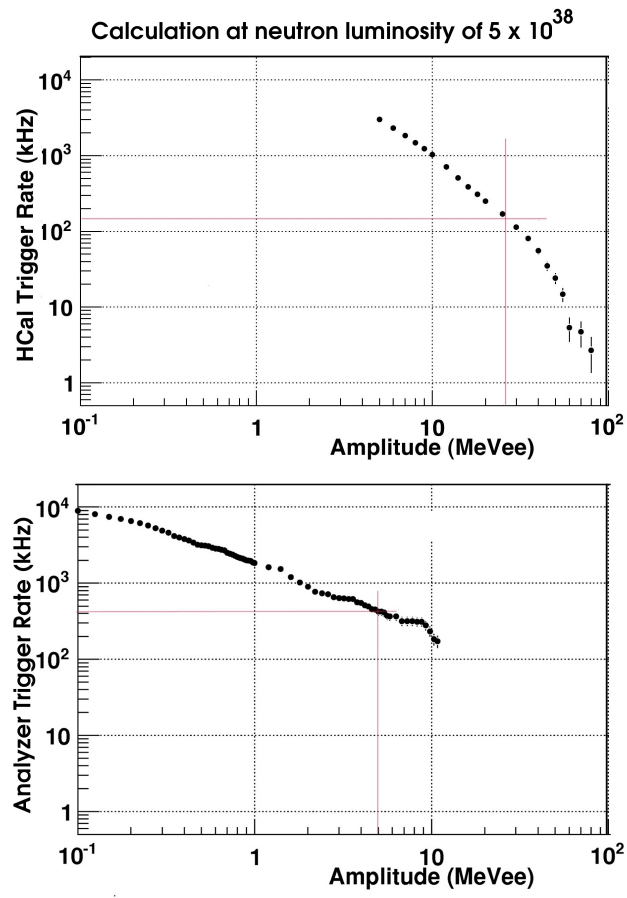


Figure 23: Simulated counting rates in the polarimeter. Top for HCal, bottom for the analyzer array. The calculation has been made at  $\mathcal{L}_n = 5 \times 10^{38} \text{ cm}^{-1} \text{ s}^{-1}$ , double that of the present proposal.

### 4.3 The Quasi-elastic Signal and Background Rejection

Inelastic processes, largely associated with pion electroproduction and quasi-elastic  ${}^2H(e, e'p)$ , constitute potential sources of background to the quasi-elastic  ${}^2H(e, e'n)$  signal. Contamination of the electron-arm, quasi-elastic (QE) event sample by charged pions is expected to be extremely small. Background processes such as pion photoproduction will be suppressed very effectively by offline cuts and should not constitute a significant source of contamination. For the nucleon momenta of interest here, QE neutrons may be separated cleanly from the equivalent protons, which are deflected by the 48D48 dipole magnet before incidence on the polarimeter (Sec.3.2.5).

In the GEn(1) experiment E02-013 [10], the selection of QE events from the inelastic background has been made on the basis of cuts on

- $p_{miss}^\perp, p_{miss}^\parallel$ , the perpendicular and parallel components of missing momentum, obtained from the neutron momentum  $\vec{p}_n$ , provided by the polarimeter hit position and time of flight, and the 3-momentum transfer  $\vec{q}$ , provided by BigBite. They are given by:  $p_{miss}^\perp = |(\vec{q} - \vec{p}_n) \times \vec{q}| / |\vec{q}|$  and  $p_{miss}^\parallel = \vec{q} \cdot (\vec{q} - \vec{p}_n) / |\vec{q}|$ .
- $W$  the invariant mass of the system comprising the virtual photon and the target neutron (assumed free and at rest), given by:  

$$W = \sqrt{m_n^2 + 2m_n(E_e - E_{e'}) - Q^2}.$$
- The missing mass in the hadronic final state also gives some additional selection capability.

The  $W$  and  $p_{miss}$  resolution of the present system has been estimated, using the position and momentum resolutions of BigBite and the polarimeter described in Sec.3.

To Summarize: the resolution of the current apparatus in reconstructing these variables was estimated on the basis of assumptions about the angular resolution ( $\sigma$ ) of BigBite ( $\delta\theta_e = 1$  mr), the momentum resolution of BigBite ( $\delta p_n/p_n = 0.5\%$ ), the (start) time resolution of BigBite ( $\delta t = 0.25$  ns), the angular resolution of the analyzer ( $\delta\theta_n = 3.5$  mr) and the time of flight resolution of the analyzer (Sec.3.2.1). Variations in flight path, due to target length and detector thickness, are accounted for and the intrinsic PMT time resolution was estimated at 0.3 ns ( $\sigma$ ). The calculation considers Fermi smearing of the QE scattering process as in Sec.3.3.

The present calculated distributions are compared with real data from GEn(1) (Fig.24). The present  $p_{miss}^\parallel$  is somewhat poorer at high momentum (bearing in mind that it is at slightly higher momentum), while the  $p_{miss}^\perp$  distributions appear broadly similar on a 2D plot. The present  $W$  distribution for  ${}^2H$  (as opposed to  ${}^3He$  in GEn(1)) is tighter.

The calculated 1D distributions of  $W$ ,  $p_{miss}^\perp$  and  $p_{miss}^\parallel$  are compared for  $Q^2 = 1.5$  and  $4.0$  (GeV/c) $^2$  in Fig.25. . As  $Q^2$  and the momentum of the recoil neutron increases, the resolution from time of flight degrades and with it the resolution of  $p_{miss}^\parallel$ . BigBite resolution gives a relatively small contribution to the widths of the distributions. The present  $p_{miss}^\perp$  distributions are confined to

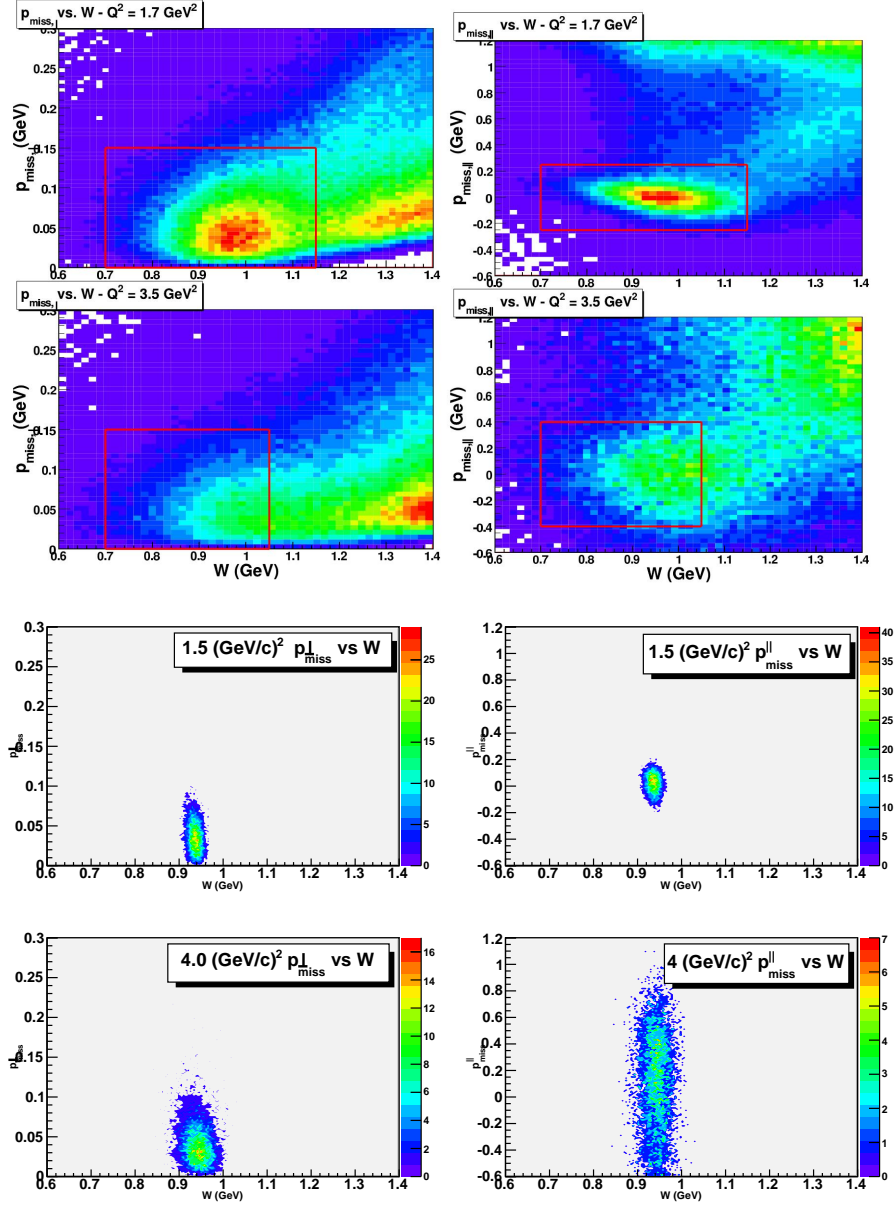


Figure 24: Top plots Left:  $P_{miss}^\perp$  and Right:  $P_{miss}^\parallel$  vs.  $W$  from experiment E02-103. The top row is for  $Q^2 = 1.7 \text{ (GeV/c)}^2$ , while the second row is for  $3.5 \text{ (GeV/c)}^2$ . The bottom plots show present calculations for  $Q^2 = 1.5 \text{ (GeV/c)}^2$  and  $4.0 \text{ (GeV/c)}^2$  in a similar sequence.

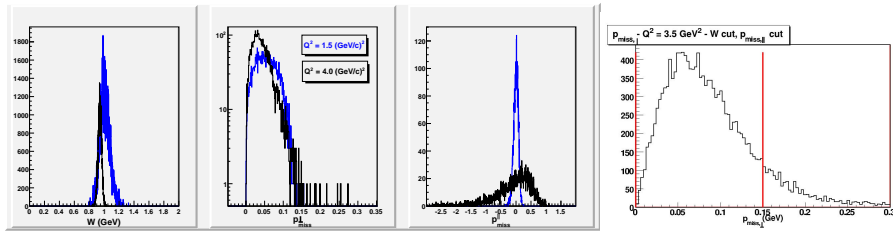


Figure 25: Left: simulated invariant Mass and missing momentum distributions at  $Q^2 = 1.5 \text{ (GeV/c)}^2$  (blue) and  $Q^2 = 4.0 \text{ (GeV/c)}^2$  (black). Right:  $p_{miss}^\perp$  distribution from GEN(1).

$p_{miss}^\perp < 0.15 \text{ GeV/c}$ , while the GEN(1) distribution has a significant tail extending to higher missing momenta.

It is expected that the present experiment, using a  $^2\text{H}$  target will have significantly better separation of the QE signal than experiments which employ a  $^3\text{He}$  target. The present experiment is similar in many respects to experiment E12-09-019 to measure  $G_M^n/G_M^p$  [7], which also employs BigBite on the electron arm and the HCAL array on the nucleon arm. It is expected that the momentum and angle resolutions are going to be very similar. In E12-009-019 the QE signal has been modeled in a similar way to the present calculations, while inelastic background was calculated using code Genev [84], smeared by Fermi motion and detector resolution. Some of these calculations at  $Q^2 = 3.5 \text{ (GeV/c)}^2$  are shown in Fig. 26 (Top). Here the acceptance averaged cross section is plotted against  $W^2$  and  $\theta_{qn}$ , the angle between the direction of the virtual photon and the direction of the recoiling neutron. The estimated systematic uncertainty in subtracting background from the QE signal is estimated to be  $\sim 2\%$ .

The distributions of  $W^2$  and  $\theta_{qn}$  for the present apparatus have been calculated for QE scattering, with smearing for detector resolution as described above. They are shown in the bottom panels of Fig. 26, which demonstrate that the worst-case widths ( $Q^2 = 6 \text{ (GeV/c)}^2$ ) of the present  $W^2$  and  $\theta_{qn}$  distributions are no broader than the displayed calculation from E12-009-019. Thus corrections for inelastic contamination will be relatively small and induced systematic uncertainties will not exceed the 2% level.

#### 4.4 Systematic Uncertainties

The most important issues associated with analysis of the systematic uncertainties are presented here. Work continues to refine these calculations.

Potential sources of experimental systematic error are :

- Beam polarization uncertainty, which cancels in a ratio measurement.
- Analyzing power uncertainty, which cancels in a ratio measurement.
- Azimuthal angle acceptance non-uniformity, which cancels after beam helicity flip and the additional check of precession angle flip.
- Variation in the effective analyzing power with azimuthal angle. The first calculations described in Sec.4.1.3 do not show any significant variations.

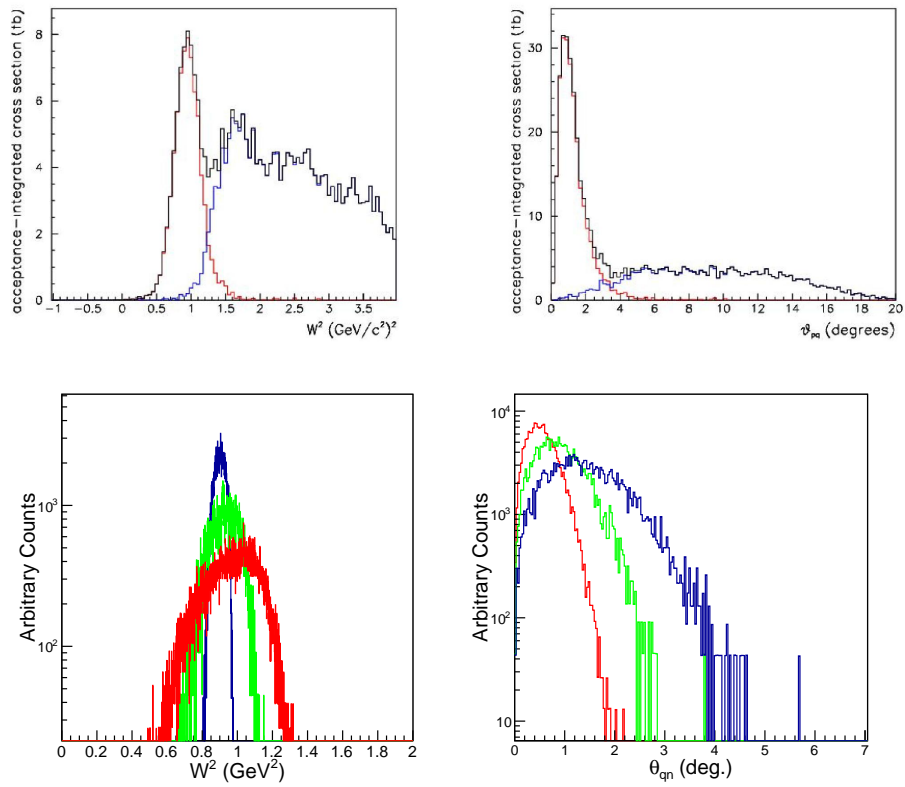


Figure 26: Top panels: Separation of quasi-elastic and inelastic events for  $d(e, e'n)$  events at  $Q^2 = 3.5$   $(\text{GeV}/c)^2$  from experiment E12-009-019 [7]. The QE signal is in red, inelastic background in blue and total in black. Bottom panels: The equivalent QE signals for the present proposal; blue  $Q^2 = 1.5$   $(\text{GeV}/c)^2$ ; green  $Q^2 = 3.0$   $(\text{GeV}/c)^2$ ; red  $Q^2 = 6.0$   $(\text{GeV}/c)^2$ . Note that the bottom panels are on a logarithmic scale.

However, potential variations in the effective analyzing power, which may be different in the  $x$  and  $y$  directions, as one scans over the full vertical and horizontal range of the analyzer, are not ruled out. If this proves to be a significant effect, then it can be corrected using the good position resolutions of the analyzer and HCAL arrays.

- Separation of  $P_x$  from  $P_z$  does not rely on variation of the magnitude of the spin-precession magnetic field. In the present experiment  $P_x$  and  $P_z(P_z \rightarrow P_y)$  are measured simultaneously with the same precession field, so that potential effects of changes to the background counting rates on the measured asymmetry are thus avoided. Non-uniformity of the magnetic field results in a small amount of  $P_z \rightarrow P_x$  mixing. Given that the analyzer array has good position resolution, the neutron path through the dipole can be reconstructed accurately and this effect corrected with an overall uncertainty of 1%.
- Reproducibility of the spin precession angle after polarity reversal. At a precession angle of  $\sim 75\%$ , a 1% difference in integrated field would give 0.25% difference in  $P_z \rightarrow P_y$ .
- The vertical distribution of counting rates in the polarimeter will change when the polarity of the spin precession dipole is reversed. Any significant effect from changes to the level of signal contamination will show up when different combinations of beam-helicity-flip and dipole-flip asymmetries are compared (Sec. 4.1.4).
- Variation in the angle of spin precession through the dipole magnet. The path of a neutron through the dipole can be reconstructed with sufficient precision that a correction factor can be evaluated event by event. The estimated uncertainty is 0.25%.
- Dilution of the asymmetry by accidental background. The background is estimated to be at the 1% level (Sec.4.2) which can be subtracted without significant error.
- Contamination of the quasi-elastic signal by inelastic processes. In GEN(1) the uncertainties arising from evaluation of the inelastic background were estimated as 1.1%, 2.7%, 6.0% at  $Q^2 = 1.7, 2.8$  and  $3.4$  (GeV/c)<sup>2</sup> respectively. A deuteron measurement will have cleaner rejection of the inelastic background. An estimate of 2% is made (Sec. 4.3), based on comparison with background estimates from experiment E12-009-019 and Monte Carlo calculations of the present QE signal.
- Dilution of the asymmetry, due to proton charge exchange (mainly in the Pb shield) upstream of the veto detectors of the analyzer array. This factor will be evaluated using data from <sup>1</sup>H, <sup>3</sup>He and <sup>12</sup>C targets. In GEN(1) the associated systematic uncertainty was between 3 and 4%. Here protons will be deflected by a dipole magnet (Fig.13) before interaction in the Pb wall and thus resultant neutrons will tend to be displaced outside of quasi-elastic data cuts. We estimate a 1% uncertainty provisionally.

Overall we estimate that a 3% systematic error is achievable.

$Q^2$	$\langle p_n^{lab} \rangle$	$\langle P_e P_x \rangle$	$\langle P_e P_z \rangle$	$\langle A_y \rangle$	$\chi^\circ$	$F^2$ $\times 10^{-4}$	$\delta P$ $\times 10^{-3}$
1.5	1.44	0.123	0.509	0.172	83	20.7	2.95
2.0	1.76	0.151	0.616	0.132	79	12.2	3.77
3.0	2.35	0.124	0.409	0.090	75	5.67	5.52
4.0	2.89	0.167	0.529	0.068	73	3.24	8.01
6.0	4.03	0.170	0.490	0.041	72	1.18	15.4

Table 6: Values of polarization parameters at the kinematic settings of the present proposal. The angle brackets denote mean values integrated over the kinematic range of a particular setting.  $\delta P$  values are quoted for the measurement times in Table 7, equivalent to  $\sim 10^8$  incident neutrons.

## 5 Proposed Measurements

### 5.1 Counting Rate Estimates

The estimate of required counts is based on the following:

1. The expected degree of polarization of the incident electrons. Previous measurements indicate that values in excess of 0.8 are generally available and we use the value 0.8 for the following estimates.
2. The acceptance of BigBite and the polarimeter for quasi elastic  ${}^2\text{H}(e, e'n)$ . The kinematic settings are given in Sec.3.3.
3. The predicted detection efficiency and acceptance of the polarimeter is based on Monte Carlo studies. The neutron detection efficiency of the analyzer will be around 20%, while the hadron calorimeter has an efficiency of around 80% for both p and n. The calculations are described in Sec.4.1.3. The overall efficiency of the polarimeter, after scattering angle selection, is around 7%.
4. The estimate of the  $n + \text{CH}$  analyzing power has been obtained using the procedure described in Sec.2.4.2. The polarimeter figure of merit and uncertainties have been obtained from Eq.13,14 which provide predictions consistent with the results of a simulation of polarized neutron scattering.

Table 6 displays parameters relevant to the precision of the polarization measurement for neutron momenta ( $p_n^{lab}$ ) associated with  $Q^2 = 1.5, 2.0, 3.0, 4.0,$  and  $6$  (GeV/c) $^2$  kinematic settings. The estimate of  $\delta P$  (Eq.14) has been made using the figure of merit  $F^2$  and the counting times of Table 7, which produce  $\sim 10^8$  incident neutrons.  $F^2$  is calculated (Eq.13) using an efficiency of 0.07, produced by the Monte Carlo simulation (Sec.4.1.3), after selection of polar scattering angles to optimize the polarimeter FoM. The parametrization of the analyzing power  $A_y^n(p_n, \theta'_n)$  is described in Sec.2.4 and the parameters  $P_x^*, P_y^*$  have been calculated using the form-factor fit of Ref.[83].

The counting rate estimate (Table 7) is based on the expected luminosity and the cross section for free  $n(e, e'n)$  scattering. The cross section has been calculated using Eq.5 and the parametrization of the  $Q^2$  dependence of the Sachs

$\langle Q^2 \rangle$ (GeV/c) <sup>2</sup>	$\langle \Omega_{e'} \rangle$ (msr)	$\langle \Omega_{e',n} \rangle$ (msr)	$\langle \sigma_n(\theta) \rangle$ (pb/sr)	Rate (Hz)	Time (hr)	$\delta R/R$ (stat)   (sys)	
1.5	58.9	49.4	1236	539	4	0.025	0.03
2.0	58.7	58.4	218	112	20	0.026	0.03
3.0	58.8	44.5	239	93.8	24	0.047	0.03
4.0	58.8	57.1	24.8	12.5	150	0.050	0.03
6.0	58.3	54.2	5.8	2.77	500	0.096	0.03

Table 7: Counting rate and error estimate for  $n(e, e'n)$  for an incident (neutron) luminosity of  $1.26 \times 10^{38} \text{ cm}^{-2}\text{s}^{-1}$ . The angle brackets denote averaging over the acceptance of the detector system. “Rate” is the detected  $n(e, e'n)$  rate which accounts for solid angle and detection efficiency.

form factors of Ref. [83]. A 10 cm LD<sub>2</sub> target has a thickness of 1.69 g/cm<sup>2</sup> which gives a (neutron) luminosity of  $1.26 \times 10^{38} \text{ cm}^{-2}\text{s}^{-1}$  for an incident beam current of 40  $\mu\text{A}$ . The Counting rate estimate assumed a polarimeter efficiency of 7%. The statistical uncertainty is estimated from Eq.22, where  $\delta P$  is given in Table 6. The systematic uncertainty of 3% is discussed in Sec.4.4.

## 5.2 Beam Time Request

Beam time is requested (Table 8) to measure  $G_E^n/G_M^n$  at five values of  $Q^2$ . The request also includes time for calibrations of the spectrometers and changes in spectrometer positions for different kinematic settings. Electron beam helicity flip is performed at 30 Hz, so that combination with the up-down polarized data will yield the effectively unpolarized azimuthal distributions in the polarimeter. At each  $Q^2$  point we will measure at two equal, but opposite polarity setting of the spin-precession dipole. This will effectively reverse the  $P_y$  (precessed from  $P_z$ ), to make the separation procedure of  $x$  and  $z$  (precessed to  $y$ ) components of the recoil-neutron polarization more robust and provide an extra check on possible instrumental effects.

In order to determine the four-momentum of the virtual photon to best accuracy, the optics of BigBite has to be well known. For each kinematic setting, data will be taken with a multi-foil carbon target and a removable sieve slit of lead, located at the front face of the magnet. These provide the means to calibrate accurately the angular coordinates before magnetic deflection and also the scattering vertex position. The momentum calibration is obtained from elastic  $e-p$  scattering from a LH<sub>2</sub> target, where the kinematics are very similar to the quasi-elastic  $e-n$  case, so that detectors do not require to be moved. Data will also be taken with a liquid <sup>3</sup>He target. In conjunction with the data taken with the other employed targets (<sup>1</sup>H, <sup>2</sup>H, <sup>12</sup>C) this will facilitate the evaluation of  $p-n$  conversion effects.

In total we request 1054 hr of CEBAF beam time. This is broken down in Table 8.

Q <sup>2</sup>	Function	Target	Precession	Time (hr)
1.5	Production $^2H(\vec{e}, e'\vec{n})$	LD <sub>2</sub>	pos	2
1.5	Production $^2H(\vec{e}, e'\vec{n})$	LD <sub>2</sub>	neg	2
1.5	BB Optics, Vertex	C Foil	-	12
1.5	Calib. $^1H(e, e'p)$	LH <sub>2</sub>		4
1.5	Calib. $^3He(e, e'p)$	L <sup>3</sup> He		4
1.5	Config Change	-		16
2.0	Production $^2H(\vec{e}, e'\vec{n})$	LD <sub>2</sub>	pos	10
2.0	Production $^2H(\vec{e}, e'\vec{n})$	LD <sub>2</sub>	neg	10
2.0	BB Optics etc.	C Foil		24
2.0	$^1H(e, e'p)$	LH <sub>2</sub>		16
2.0	Calib. $^3He(e, e'p)$	L <sup>3</sup> He		16
2.0	Config Change	-		16
3.0	Production $^2H(\vec{e}, e'\vec{n})$	LD <sub>2</sub>	pos	12
3.0	Production $^2H(\vec{e}, e'\vec{n})$	LD <sub>2</sub>	neg	12
3.0	BB Optics etc.	C Foil		24
3.0	$^1H(e, e'p)$	LH <sub>2</sub>		24
3.0	Calib. $^3He(e, e'p)$	L <sup>3</sup> He		24
3.0	Config Change	-		16
4.0	Production $^2H(\vec{e}, e'\vec{n})$	LD <sub>2</sub>	pos	75
4.0	Production $^2H(\vec{e}, e'\vec{n})$	LD <sub>2</sub>	neg	75
4.0	BB Optics etc.	C Foil		24
4.0	$^1H(e, e'p)$	LH <sub>2</sub>		24
4.0	Calib. $^3He(e, e'p)$	L <sup>3</sup> He		24
4.0	Config Change	-		16
6.0	Production $^2H(\vec{e}, e'\vec{n})$	LD <sub>2</sub>	pos	250
6.0	Production $^2H(\vec{e}, e'\vec{n})$	LD <sub>2</sub>	neg	250
6.0	BB Optics etc.	C Foil		24
6.0	$^1H(e, e'p)$	LH <sub>2</sub>		24
6.0	Calib. $^3He(e, e'p)$	L <sup>3</sup> He		24
Total				1054

Table 8: Breakdown of beam time request

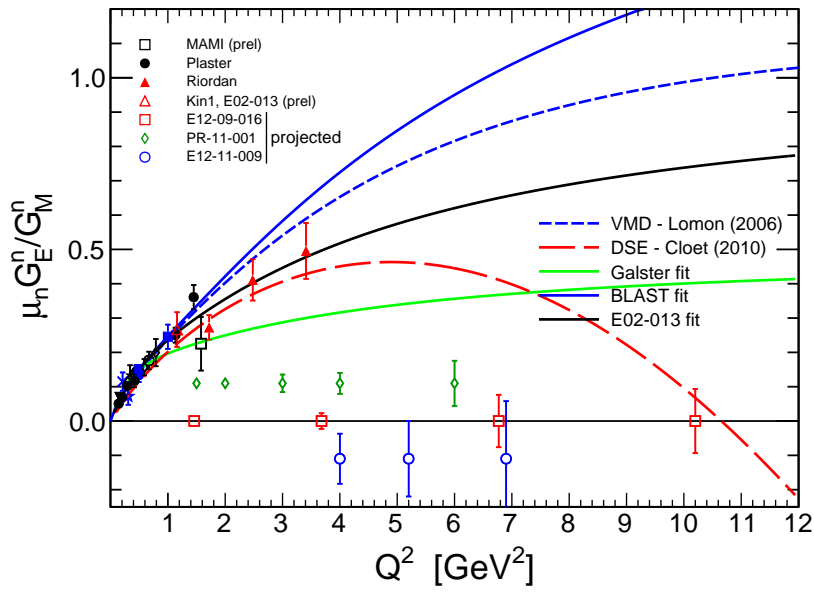


Figure 27: Comparison of the projected absolute uncertainties of this proposal (green diamonds), proposal E12-09-016 [6] (red squares) and proposal E12-11-009 [59] (blue circles). Also shown are previous measurements and some theoretical curves. The E12-11-009 uncertainties are as given in that proposal. However, our present analysis (see Sec.2.4.2) predicts that E12-11-009 has over estimated the analyzing power of their polarimeter. We predict that the error bar will expand by a factor 1.7 at the E12-11-009  $Q^2$  point of  $6.88 \text{ (GeV/c)}^2$  (for which 720 hr was requested).

## 6 Summary

We propose to measure the ratio  $G_E^n/G_M^n$  from a double-polarization asymmetry, using the longitudinally polarized CEBAF electron beam and a polarimeter to measure the transfer of polarization to the recoiling neutron in quasi-elastic  ${}^2\text{H}(\vec{e}, e' \vec{n})$ . The measurement will be made at five values of the squared four-momentum transfer of the scattered electron:  $Q^2 = 1.5, 2.0, 3.0, 4.0$  and  $6.0$   $(\text{GeV}/c)^2$ . It aims to achieve relative uncertainties (statistical + systematic in quadrature) in the ratio  $G_E^n/G_M^n$  between 4 and 10%. Systematic effects for this  ${}^2\text{H}(\vec{e}, e' \vec{n})$  experiment are well under control (estimated 3% systematic uncertainty) and the use of a highly efficient polarimeter results in excellent precision. Relative statistical uncertainties are estimated (using the BLAST parametrisation of  $G_E^n$ ) to be 2.5 - 10%.

This level of accuracy will exercise very powerful constraints on the form factor behavior at moderate  $Q^2$ , as well as providing an independent check of other  $G_E^n/G_M^n$  measurements, which use polarized-target techniques. We note that a new proposal [85] to PAC 39 seeks to measure  $G_E^n$  in the range  $Q^2 = 1 - 2.6$   $(\text{GeV}/c)^2$  to high precision, using an alternative technique: inclusive  ${}^3\vec{H}e(\vec{e}, e')$  scattering.

Fig. 27 compares the projected absolute uncertainties of the present proposal with those of E12-009-016 [6] and E12-11-009 [59]. Clearly the present data would represent a major advance in constraining form factor behavior at medium momentum transfer. Here the sensitivity to structural effects, such as di-quark configurations, will be most pronounced and already the predictions of theoretical models are diverging rapidly. The uncertainties in  $G_E^n$  largely determine the precision obtainable in a flavor decomposition of the  $F_1$  and  $F_2$  form factors. Di-quark structure effects are expected to show up in divergent  $u$ - and  $d$ -quark behaviour (Fig. 3) from  $Q^2 \gtrsim 1.5$   $(\text{GeV}/c)^2$ . To establish this behaviour it is vital to have the best possible measurements of  $G_E^n$ . Bearing in mind that  $G_E^n/G_M^n$  by recoil polarimetry in quasi-free  ${}^2\text{H}(\vec{e}, e' \vec{n})$  has not been measured previously beyond  $1.5$   $(\text{GeV}/c)^2$ , the present experiment represents the best means to establish the flavor decomposed distributions in the medium  $Q^2$  region.

It is also important to extend the range of  $Q^2$  measurements as far as possible and the present experiment will measure up to  $Q^2 = 6.0$   $(\text{GeV}/c)^2$ . There the overall uncertainty achievable by the present experiment is significantly better than E12-11-009. If the analyzing power of the neutron polarimeter in E12-11-009 is obtained using the procedure employed in this proposal (Sec.2.4), the E12-11-009 error bars (blue data points Fig. 27) expand by factors 1.3, 1.4 and 1.7 at  $Q^2$  values 3.95, 5.22 and 6.88 respectively, and the advantage of the present proposal is further emphasized.

The use of a  ${}^2\text{H}$  target, as opposed to  ${}^3\text{He}$ , enables much cleaner separation of the elastic signal from inelastic background. Background subtraction uncertainties in  ${}^3\vec{H}e(\vec{e}, e' n)$  constitute a major part of the systematic uncertainty in E12-09-016 and the present  ${}^2\text{H}(\vec{e}, e' \vec{n})$  measurement has a considerable advantage in this respect.

Recoil neutron polarimetry is relatively unknown territory in terms of the neutron analyzing power of organic materials. We have thus limited our beam request to  $Q^2 \leq 6$   $(\text{GeV}/c)^2$  where we believe that good accuracy and precision

can be achieved in a reasonable time.

## The Collaboration

This experiment will be performed in Hall-A of Jefferson Laboratory and has been approved as a Hall-A collaboration experiment. It will be part of the SBS program of experiments and much of the apparatus necessary for this experiment (BigBite, the SBS dipole, HCAL) will be used in other experiments. The joint international effort encompasses groups from the USA (JLab, UVa, CMU, W&M, CSU, NSU), the UK (Glasgow), Italy (INFN Catania and Rome), The Russian Federation (JINR Dubna) and Canada (St. Mary's).

We list the institutes which are most directly involved in building the apparatus required by the present experiment .

- **Jefferson Laboratory:**

The Hall A group will take on the design of the apparatus layout, the modification of the 48D48 magnet and beam-line vacuum pipe. The group will be responsible for the installation and commissioning of the upgraded infrastructure required for the magnet, the targets, the beam line and the BigBite electron spectrometer. JLab have negotiated with SLAC the transfer of 6000 photomultipliers (originally used for BaBar) for use in BigBite and the SBS.

- **University of Glasgow:**

The University of Glasgow have initiated R&D on the polarimeter and have a Ph.D. student working on this investigation. They are responsible for the new BigBite timing hodoscope, design and implementation of the analyzer scintillator array and design of the front-end electronics for the (former BaBar) PMTs used in BigBite and SuperBigBite. They will also build the smaller scale, prototype polarimeter for measurements of analyzing power at Dubna.

- **JINR Dubna:**

Dubna are responsible for construction of the modules of HCAL the hadron calorimeter. They will lead the effort to measure the analyzing power of neutron scattering from plastic scintillator at neutron momenta of several GeV/c. This will use the polarized neutron beam produced by the Nuklotron accelerator in Dubna. They will ensure the necessary provision of beam and infrastructure to carry out the measurement and will supply HCAL modules for the prototype polarimeter.

- **INFN Catania:**

The Catania group will participate in the R&D, procurement and assembly work on the neutron polarimeter. They will be responsible for the implementation of the analyzer scintillator array and the forward array of veto scintillator tiles, which provide particle identification information.

- **INFN Rome:**

The Rome group are leading the effort to build the front tracker GEM chambers, used in BigBite, and also the design and implementation of the

GEM readout electronics. These detectors also form the forward trackers of the SBS proton polarimeter and will benefit all experiments which use the common apparatus.

- **University of Virginia:**

The UVA group are leading the effort to build the large rear GEM chambers, used in BigBite, and are also heavily engaged in chamber R&D work. These detectors also form the rear trackers of the SBS proton polarimeter and will benefit all experiments which use the common apparatus.

- **Carnegie Mellon University:**

The CMU group lead the R&D effort on the hadron calorimeter modules, which involves optimization of the pulse height response and improvement of time resolution. HCAL will be the high efficiency nucleon detector for several SBS experiments and will benefit all experiments which use the common apparatus.

- **St. Mary's University:**

The St. Mary's group are building the coordinate detector, which will sit before the hadron calorimeter and provide charged particle identification and vetoing capability. This detector is being designed initially for the electron arm of the GEp(5) experiment, but it is also suitable for use with HCAL and will benefit all experiments which use the common apparatus.

- **College of William and Mary:**

The W&M group will build the new gas Cherenkov detector for BigBite, which will provide more selective triggering on electrons, as well as improved  $e^- - \pi^-$  separation. This work will benefit all experiments which use BigBite.

- **California State University:**

The California State group are providing workshop facilities for the manufacture of PMT housings which exclude He from the PMT.

- **Norfolk State University:**

The Norfolk State group are active in the effort to build the new coordinate detector and lead the effort to test the 634 multianode PMTs obtained from FNAL, which will be suitable for scintillator readout via optical fibers.

## Cost Estimate of the Polarimeter Analyzer

The major new piece of apparatus required by this proposal is the array of plastic scintillators which form the active analyzer block of the neutron polarimeter. The array consists of 864 bars of plastic scintillator. The realization of this array is planned as follows.

- New plastic scintillator bars would cost \$45,000. Glasgow already have a stock of 100 of these bars.
- The PMT's would be tubes employed previously on the DIRC systems of BaBar. There are in excess of  $10^4$  of these PMT's and 3000 have already

been transferred to JLab. A further 3000 are expected to be transferred to JLab in 2012.

- The PMT voltage divider, anode pulse fast amplifier and timing discriminator are designed by the Glasgow group. A 16-channel front-end amplifier/discriminator card is under development and at  $\sim$  \$250 per card would cost  $\sim$  \$27000 to equip the full array of analyzer and veto scintillators. JLab already have the NINO chips, on which the cards are based. This card will also be used for PMT readout in BigBite and other components of the SBS. Voltage dividers would amount to  $\sim$  \$4000.
- Veto counter scintillator and readout fibres would cost in the region \$20,000.
- The veto counters would use multi-anode PMTs obtained from FNAL, as also employed on the coordinate detector.
- Analogue to digital conversion (both pulse height and time) will use existing hardware within the Hall-A and SBS collaborations.
- The mechanical mounting, including the provision to incorporate shielding is estimated to cost \$10000.

## References

- [1] G.D. Cates, C.W. De Jager, S. Riordan and B. Wojtsekhowski, Phys. Rev. Lett. 106(2011), 252003.
- [2] R. Hofstadter, Rev. Mod. Phys. 28(1956), 214.
- [3] J.J. Kelly, Phys. Rev. C66(2002), 065203.
- [4] G.A. Miller, Phys. Rev. Lett. 99(2007), 112001.
- [5] M. Vanderhaeghen and Th. Walcher, Nucl. Phys. News 21(2011), 14.
- [6] *Measurement of the Neutron Electromagnetic Form Factor Ratio  $G_E^n/G_M^n$  at High  $Q^2$* , JLab Experiment E12-09-016, Spokespersons: G. Cates, S. Riordan, B. Wojtsekhowski.
- [7] *Precision Measurement of the Neutron Magnetic Form Factor at to  $Q^2 = 18$  (GeV/c) $^2$* . Jefferson Lab experiment E12-09-019, Spokespersons: J. Annand, R. Gilman, B. Quinn, B. Wojtsekhowski,
- [8] *Large Acceptance Proton Form Factor Ratio Measurements at 13 and 15 (GeV/c) $^2$  Using Recoil Polarization Method*, JLab Experiment E12-07-109, Spokespersons: E. Brash, E. Cisbani, M. Jones, C.F. Perdrisat, L.P. Pentchev, V. Punjabi, B. Wojtsekhowski.
- [9] *Precision Measurement of the Proton Elastic Cross Section at High  $Q^2$* , JLab. experiment E12-07-108, Spokespersons: J. Arrington, S. Gilad, B. Moffit, B. Wojtsekhowski.

- [10] S. Riordan *et al.*, Jefferson Lab experiment E02-013, Phys. Rev. Lett. 105(2010), 262302.
- [11] B. Plaster *et al.*, Phys. Rev. C73(2006), 025205.
- [12] M.K. Jones *et al.* Phys. Rev. Lett. 84(2000), 1398.
- [13] S.J. Brodsky, G.R. Farrar, Phys. Rev. D11(1975), 1309.
- [14] O. Gayou *et al.*, Phys. Rev. Lett. 88(2002), 092301.
- [15] V. Punjabi *et al.*, Phys. Rev. C71(2005), 055202.
- [16] A. Puckett *et al.*, Phys. Rev. C104(2010), 242301.
- [17] L. Andivahis *et al.*, Phys. Rev. D50(1994), 5491.
- [18] M.E. Christy *et al.*, Phys. Rev. C70(2004), 015206.
- [19] I.A. Qatten *et al.*, Phys.Rev.Lett. 94(2005), 142301.
- [20] A.V. Belitsky, X. Ji and F. Yuan, Phys. Rev. Lett. 91(2003), 092003.
- [21] B. Wojtsekhowski, Private Communication, Nov. 2010.
- [22] J.J. Kelly, Phys. Rev. C70(2004), 068202.
- [23] C.D. Roberts and A. G. Williams, Prog. Part. Nucl. Phys. 33(1994), 477.
- [24] I.C. Cloët *et al.*, Few Body Syst., 46(2009), 1.
- [25] C.D. Roberts, arXiv: 1203.5341v1 [nucl-th], March 2012, and references therein.
- [26] M.R. Frank, B.K. Jennings and G.A. Miller, Phys. Rev. C54(1996), 920.
- [27] G.A. Miller and M. R. Frank, Phys. Rev. C65(2002), 065205.
- [28] G.A. Miller, Phys. Rev. C66(2002), 032201 R.
- [29] C.D. Roberts *et al.*, Eur. J. Phys. ST 140(2007), 53.
- [30] H.H. Matevosyan, A.W. Thomas and G.A. Miller, Phys. Rev. C72(2005), 065204.
- [31] M. Diehl *et al.*, Eur. J. Phys. C39(2005), 1.
- [32] M. Gockeler *et al.*, (QCDSF/UKQCD), PoS LAT2007(2007),161, arXiv:0710.0422 [hep-lat].
- [33] H.W. Lin *et al.*, arXiv:1005.0799v1 [hep-lat], 5th May 2010.
- [34] X. Ji, Ann. Rev. Nucl. Part. Sci. 54(2004), 413.
- [35] A.V. Belitsky and A.V. Radyushkin, Phys. Rep. 418 (2005), 1.

- [36] X. Zheng et al. Phys. Rev. C70(2004), 065207.
- [37] A. Airapetian *et al.*, Phys. Rev. Lett. 94(2005), 012002.
- [38] V. Yu. Alexakhin *et al.*, Phys. Rev. Lett. 94(2005), 202002.
- [39] *Measurement of the Single Target-Spin Asymmetry in Semi-Inclusive  $\bar{n}(e, e'\pi^-)$  Reaction on a Transversely Polarized Target*, JLab Experiment E06-010, Spokespersons: J.-P. Chen, X. Jiang, J.-C. Peng.
- [40] *Target Single Spin Asymmetry in Semi-Inclusive Deep-Inelastic  $(e, e'\pi^+)$  Reaction on a Transversely Polarized  $^3\text{He}$  Target*, JLab Experiment E06-011, Spokespersons: E. Cisbani, H. Gao, X. Jiang.
- [41] *Measurement of the Semi-Inclusive pi and kappa electro-production in DIS regime from transversely polarized  $^3\text{He}$  target with the SBS@BB spectrometers in Hall A*, JLab Experiment E12-09-018, Spokespersons: G. Cates, E. Cisbani, G. Franklin, B. Wojtsekhowski.
- [42] *An update to PR12-09-014: Target Single Spin Asymmetry in Semi-Inclusive Deep-Inelastic Electro Pion Production on a Transversely Polarized  $^3\text{He}$  Target at 8.8 and 11 GeV*, JLab Experiment E12-10-006, Spokespersons: J.P. Chen, H. Gao, X. Jiang, J.C. Peng, X. Qian.
- [43] A. Adare *et al.* Phys. Rev. D76(2007), 051106(R).
- [44] E.L. Lomon, Phys. Rev. C66(2002), 045501.
- [45] E.L. Lomon, arXiv:nucl-th/0609020, September 2006.
- [46] R. Bijker and F. Iachello, Phys. Rev. C69(2004), 068201.
- [47] A.I. Akhiezer *et al.*, JEPT 33(1957), 765.
- [48] R.G. Arnold *et al.*, Phys. Rev. C23(1981), 36.
- [49] N.V. Vlasov *et al.*, Instr. and Exp. Tech. 49(2006), 49.
- [50] R. Diebold *et al.*, Phys. Rev. Lett. 35(1975), 632.
- [51] S.L. Kramer *et al.*, Phys. Rev. D17(1978), 1709.
- [52] *Analyzing Power of pp and np Elastic Scattering at Momenta between 2000 and 6000 GeV/c and Polarimetry at LHE*, V.P. Ladygin, JINR report E13-99-123, 1999.
- [53] A. de Lesquen *et al.*, Eur. J. Phys. C11(1999), 69
- [54] CNS Center for Nuclear Studies, SAID Partial Wave Analysis, R. Arndt et al., <http://gwdac.phys.gwu.edu/>.

- [55] H. Spinka *et al.*, Nucl. Instr. and Meth. A211(1983), 239.
- [56] L.S. Azhgirey *et al.*, Nucl. Instr. and Meth. A538(2005), 431.
- [57] N.E. Cheung *et al.*, Nucl. Instr. and Meth. A363(1995), 561.
- [58] I.G. Alekseev *et al.*, Nucl. Instr. and Meth. A434(1999), 254.
- [59] *The Neutron Electric Form Factor at  $Q^2$  up to 7 (GeV/c) $^2$  from the reaction  ${}^2\text{H}(\bar{e}, e'\bar{n})$  via Recoil Polarimetry.* JLab. Experiment E12-11-009, Spokespersons: B.D. Anderson, J. Arrington, S. Kowalski, R. Madey, B. Plaster, A. Yu. Semenov.
- [60] I. Passchier *et al.*, Phys. Rev. Lett. 82(1999), 4988.
- [61] H. Zhu. Phys. Rev. Lett. 87(2001), 081801.
- [62] C. Herberg *et al.*, Eur. J. Phys. A5(1999), 131.
- [63] J.Becker *et al.*, Eur. J. Phys. A6(1999), 329.
- [64] D.Rohe *et al.*, Phys. Rev. Lett. 83(1999), 4257.
- [65] B.S. Schlimme, Proc. SPIN2010, J. Phys.: Conf. Ser. 295 (2011), 012108.
- [66] T. Eden *et al.*, Phys. Rev. C50(1994), 1749.
- [67] M. Ostrick *et al.*, Phys. Rev. Lett. 83(1999), 276.
- [68] D.I. Glazier *et al.*, Eur. J. Phys. A24(2005), 101.
- [69] G. Warren *et al.*, Phys. Rev. Lett. 92(2004), 042301.
- [70] J. Lachniet *et al.*, Phys. Rev. Lett. 102(2009), 192001.
- [71] S. Rock *et al.*, Phys. Rev. D46(1992), 24.
- [72] *Measurement of the Neutron Magnetic Form Factor at High  $Q^2$  Using the Ratio Method on Deuterium*, JLab experiment E12-07-104, Spokespersons: W. Brooks, G. Gilfoyle, J. Lachniet, M. Vineyard.
- [73] B. Ketzer *et al.*, Nucl. Instr. and Meth. A535(2004), 314.
- [74] *Measurement of the Analyzing Power of Polarized Neutron Scattering on Organic Scintillator at Incident Momenta of Several GeV/c*, JINR PAC Proposal (in preparation), Spokespersons: J.R.M. Annand, N.M. Piskunov, B. Wojtsekhowski.
- [75] Eljen Technology, <http://www.eljentechnology.com/>
- [76] *The DIRC Particle Identification System for the BaBar Experiment*, I Adam *et al.*, SLAC-PUB-10516, June 2004.
- [77] *Coordinate Detector Status Update*, M. Khandaker, Presentation to SBS Meeting, 18th April 2012.

- [78] TOSCA/Opera-3D, Vector Fields Software, Cobham Technical Services, Dorset, UK
- [79] *A Geant-4 Based Monte Carlo of SBS*, J.R.M. Annand, University of Glasgow 2010.
- [80] *Measurement of the Neutron Electric Form Factor at  $Q^2 = 0.8 (\text{GeV}/c)^2$* , D.I. Glazier, Ph.D. Thesis, University of Glasgow, 2003. <http://www.nuclear.gla.ac.uk/npe-theses>
- [81] *HCAL for SuperBigBite*, F.Benmokhtar, IV SuperBigBite Spectrometer Meeting, JLab, March 19, 2010.
- [82] P.V. Degtyarenko, computer code DINREG, *Applications of the Photonuclear Fragmentation Model to Radiation Protection Problems*, Proc. Second Specialist Meeting on Shielding Aspects of Accelerators (SATIF2), CERN, October 1995.
- [83] E. Geis *et al.*, Phys. Rev. Lett. 101(2008), 042501.
- [84] M. Ripani and E.M. Golovach, Program Genev, INFN Genoa 1994. Based on P. Corvisiero *et al.*, Nucl. Instr. and Meth. A346 (1994), 433
- [85] *Measurements of  $A_{\parallel}$  and  $A_{\perp}$  to Extract  $G_E^n$  and  $G_M^n$  at  $Q^2 = 1 - 2.6 (\text{GeV}/c)^2$  from the Inclusive  ${}^3\vec{H}e(\vec{e}, e')$  Reaction*, Proposal to JLab PAC 39, Spokespersons: T. Averett, D.W. Higinbotham, V. Sulkosky and B.E. Norum.